Mechanistic Insights into MinD Regulation and Pattern Formation in *Bacillus subtilis*

Helge Feddersen[1] and Marc Bramkamp[1,*]

[1] *Institute for General Microbiology, Christian-Albrechts-University Kiel, Am Botanischen Garten* 1-9, 24118 Kiel, Germany

Running title: MinD dynamics in *B. subtilis*

*To whom correspondence should be addressed: Marc Bramkamp, Christian-Albrechts-University Kiel, Institute for General Microbiology, Am Botanischen Garten 1-9, 24118 Kiel, Germany, Email: bramkamp@ifam.uni-kiel.de; Phone: +49 (0)431-880-4341; Telefax: +49(0)431-880-2198
Twitter: @BramkampLab

Abstract

Bacteria precisely regulate the place and timing of their cell division. One of the best-understood systems for division site selection is the Min system in *Escherichia coli*. In *E. coli*, the Min system displays remarkable pole-to-pole oscillation, creating a time-averaged minimum at the cell's geometric center, which marks the future division site. Interestingly, the Gram-positive model species *Bacillus subtilis* also encodes homologous proteins: the cell division inhibitor MinC and the Walker-ATPase MinD. However, *B. subtilis* lacks the activating protein MinE, which is essential for Min dynamics in *E. coli*. We have shown before that the *B. subtilis* Min system is highly dynamic and quickly relocalizes to active sites of division. This raised questions about how Min protein dynamics are regulated on a molecular level in *B. subtilis*. Here, we show with a combination of *in vitro* experiments and *in vivo* single-molecule imaging that the ATPase activity of *B. subtilis* MinD is activated solely by membrane binding. Additionally, both monomeric and dimeric MinD bind to the membrane, and binding of ATP to MinD is a prerequisite for fast membrane detachment. Single-molecule localization microscopy data confirm membrane binding of monomeric MinD variants. However, only wild type MinD enriches at cell poles and sites of ongoing division, likely due to interaction with MinJ. Monomeric MinD variants and locked dimers remain distributed along the membrane and lack the characteristic pattern formation. Single-molecule tracking data further support that MinD has a freely diffusive population, which is increased in the monomeric variants and a membrane binding defective mutant. Thus, MinD dynamics in *B. subtilis* do not require any unknown protein component and can be fully explained by MinD's binding and unbinding kinetics with the membrane. The generation of MinD patterns relies on the short-lived temporal residence of MinD dimers at the membrane.

Keywords

B. subtilis, Min system, cell division, ATPase, membrane binding, protein patterns, reaction diffusion, self-organization, SMLM, SMT

47 ## Introduction

48 All cells face two fundamental challenges during their cycle: controlling the number of
49 divisions and ensuring these divisions occur at the correct site. While these processes are
50 extensively-studied in eukaryotes (1, 2), there remains significant uncertainty in bacterial cells.
51 Most bacteria have simple morphologies, such as cocci or rod-shaped cells, and divide by
52 binary fission. This division is governed by a complex protein machinery known as the divisome
53 (3-5). The divisome's spatial organization is directed by the dynamic arrangement of a
54 bacterial tubulin homolog, FtsZ (6, 7). FtsZ forms treadmilling protofilaments that condense at
55 the division site (8-10), recruiting several cell wall synthesis proteins, such as division-specific
56 transglycosylases and transpeptidases (11, 12). Together, these proteins synthesize the
57 bacterial peptidoglycan cell wall. The inward-growing cell wall eventually separates the two
58 daughter cells. Importantly, cell wall synthesis during cytokinesis is coupled with DNA
59 replication and segregation, ensuring the genomes are faithfully segregated into daughter
60 cells (13, 14). In rod-shaped model bacteria like *Escherichia coli* and *Bacillus subtilis*, division
61 site selection is governed by two protein systems (15-17): nucleoid occlusion and the Min
62 system. The nucleoid occlusion system prevents cytokinesis and septum closure over the
63 condensed DNA within the nucleoid (18). In *E. coli*, the nucleoid occlusion protein SlmA protein
64 binds to the nucleoid, inhibiting FtsZ polymerization (19-21). In *B. subtilis*, the unrelated ParB-
65 like protein Noc conveys the nucleoid occlusion effect (22-25).

66 The second division regulating system is the Min system. The Min system was identified by
67 the formation of small, round, anucleate cells that seemingly divided close to the cell poles
68 (26). The gene locus responsible for the "*min*iature" cell phenotype in *E. coli* was termed *minB*
69 (27, 28). Sequence analysis later revealed that the *minB* locus contains three structural genes,
70 *minC*, *minD* and *minE* (29). MinC is the actual inhibitor of FtsZ polymer formation (30, 31). The

71 MinC protein contains an N- and C-terminal domain (32) and both have been implicated with
72 FtsZ inhibition. The C-terminal domain of MinC binds to the C-terminal tail of FtsZ and the N-
73 terminal domain of MinC (33, 34), which is also responsible for dimerization, binds at the
74 interface of two FtsZ subunits (35). MinC mediated inhibition of FtsZ was also confirmed in *B.*
75 *subtilis* (36-38), suggesting a similar mechanism for cell division regulation in *E. coli* and *B.*
76 *subtilis*.

77 The spatial localization of MinC is regulated by MinD, a Walker-type ATPase that belongs to
78 the ParA/MinD family of proteins (36, 39, 40). These partitioning ATPases are involved in
79 positioning cargo within bacterial cells (41, 42). While the molecular details of partitioning and
80 positioning differ among various ParA-like proteins, a common factor is that they use binding
81 to a large surface within the bacterial cell as a template for their positioning activity (41, 42).
82 ParA proteins bind non-specifically to DNA, covering the nucleoid and exploiting it as a spatial
83 track for positioning their cargo (43). In contrast, MinD proteins bind to the membrane surface
84 via an amphipathic helix (44, 45). Membrane binding of *E. coli* MinD depends on ATP binding
85 and subsequent dimerization (39). Dimerized MinD recruits MinC and activates it to prevent
86 FtsZ dynamics (46). In *E. coli*, MinE further regulates MinD localization. MinE binds to the
87 membrane and interacts with MinD, stimulating ATP hydrolysis, which leads to the release of
88 MinD from the membrane. Slow nucleotide exchange within cytosolic MinD leads to an
89 oscillatory cycle of MinD binding and detachment, resulting in a pole-to-pole oscillation of the
90 MinCD proteins (47-49). This oscillatory behavior creates a temporal minimum of MinC
91 molecules at the precise cell center, thus licensing this area for FtsZ ring condensation and cell
92 division. This oscillatory behavior is crucial for proper cell division and can be reproduced in
93 vitro on planar membranes, demonstrating the robustness of this self-organizing system (50).

94 In the Gram-positive model bacterium *B. subtilis* homologs of MinC and MinD are encoded
95 (51, 52). Deletion of the respective genes also leads to minicell formation and hence, a role
96 for the Min system similar to the case in *E. coli* has been proposed for *B. subtilis* (36, 53).
97 However, a homolog of MinE is missing in *B. subtilis* and cell biological observation revealed
98 that the *B. subtilis* Min system does not oscillate from pole to pole (36, 53). Rather, static
99 fluorescence imaging revealed an enrichment of MinD at the cell poles and at active division
100 sites. Early genetic and cell biological analysis revealed that the polar scaffold protein DivIVA
101 is required for polar MinD localization in *B. subtilis* (36). The interaction of DivIVA and MinD is
102 mediated by the intermembrane protein MinJ (54, 55). MinJ was also shown to be part of the
103 divisome and interacts with several division proteins (55). MinJ also seems to play a role in
104 divisome disassembly, since proteins such as FtsL and PBP2b remain associated with the young
105 cell pole after division completion in mutant strains lacking MinJ (56). This function of the *B.*
106 *subtilis* Min system is also supported by recent findings that MinD is involved in FtsZ polymer
107 disassembly at the cell poles and deletion of *minD* inhibits polar peptidoglycan remodeling
108 (57).

109 We have recently shown that all component of the *B. subtilis* Min system, including DivIVA
110 and MinJ dynamically localize within the bacterial cell (56, 58-60). Interestingly, even the
111 scaffold protein DivIVA, which is highly conserved in many Gram-positive phyla, is not static
112 associated with the cell pole, but dynamically redistributes along the plasma membrane from
113 poles to septa (58-60).The dynamics of closely related DivIVA species in actinobacteria show
114 a drastically reduced mobility, in line with their function in apical growth (59). Therefore, a
115 long-standing question in the field was why the *B. subtilis* Min system retained its dynamic
116 localization. In particular, the role of the *B. subtilis* MinD ATPase cycle remained elusive, and
117 the field has been searching for a potential ATPase-stimulating protein that could replace the

118 role of the *E. coli* MinE protein for years. To address this question, we performed an in-depth
119 *in vitro* analysis of *B. subtilis* MinD and studied its ATP hydrolysis and membrane-binding
120 kinetics. Surprisingly, we found that the stimulation of ATP hydrolysis requires only MinD
121 membrane binding, with no need for an additional activating protein. Furthermore, studies
122 with various MinD mutant variants showed that *B. subtilis* MinD binds to the membrane in
123 both its monomeric and dimeric forms, in contrast to the *E. coli* MinD homolog. We confirmed
124 these findings *in vivo* using state-of-the-art single-molecule localization microscopy (SMLM)
125 and single-molecule tracking (SMT). MinD dimers seem to be stabilized by MinJ at cell poles
126 and the site of ongoing division, as judged by average localization of mutants using SMLM.
127 Importantly, all fusion proteins were expressed as allelic replacements, resulting in native
128 copy numbers of the analyzed proteins, a prerequisite for precise *in vivo* dynamics
129 determination. This work reveals that the *B. subtilis* Min system does not require any
130 unidentified components. Min dynamics can be fully explained by the current data, providing
131 new insights into the mechanisms of cell division in *B. subtilis*.

132

133 # Results
134

135 Since localization and function of MinD appear to be strongly tied to its ATPase activity, the
136 first logical step in describing and understanding details of the ATPase cycle was identification
137 of the relevant biochemical characteristics, to eventually be able to correlate these properties
138 to *in vivo* observations.

139 **Purification and gel filtration of His-MinD**

140 To this end, *B. subtilis minD* was cloned into a pET28a expression vector to obtain an N-
141 terminally His-tagged fusion protein, since C-terminal MinD fusions have been shown to
142 interfere with membrane binding (61). Recombinant His-MinD was then purified from the
143 soluble fraction of *E. coli* lysate (Fig. S 1). Since MinD is notorious for being membrane-
144 associated and thus complicating the purification effort, a well-established *E. coli* MinD
145 purification protocol was adapted (62), where buffers were supplied with excess Mg^{2+}-ADP to
146 potentially reduce MinD membrane interaction. Purification included Ni-NTA affinity
147 chromatography followed by gel filtration of the pooled, concentrated sample. Based on the
148 gel filtration chromatogram, His-MinD is still able to dimerise, as evidenced by two elution
149 peaks corresponding to the expected sizes of the monomeric (~31 kDa) and dimeric forms
150 (~62 kDa, Fig. S 1 and Fig. S 2). Furthermore, the ability of His-MinD to form larger oligomers
151 or aggregates was suggested by western blotting, where presence of His-MinD in minor peaks
152 of faster eluting fractions could be observed (Fig. S 1). Unfortunately, the Mg^{2+}-ADP excess in
153 the purification buffers did not seem to stop His-MinD membrane interaction, as a significant
154 fraction of the recombinant protein were later detected to be lost in the cell pellet. However,
155 sufficiently high His-MinD concentrations could be obtained to proceed with biochemical
156 analysis.

157 ***B. subtilis* MinD displays full ATPase activity when incubated with ATP and liposomes.**

158 Being able to purify His-MinD allowed us to investigate the biochemical conditions affecting
159 the MinD ATPase cycle next. For this purpose, we choose to use the commercially available
160 enzyme coupled EnzChek™ phosphate assay kit (Thermo Fisher Scientific). Briefly, it allows a
161 rapid and sensitive detection of phosphate released during ATPase reactions. In the presence
162 of inorganic phosphate, a purine nucleoside phosphorylase (PNP) converts a substrate (MESG)
163 into a product exhibiting a spectrophotometric shift in maximum absorption from 330 nm to
164 360 nm, allowing a colorimetric determination of free phosphate levels in an effective range
165 between 2 and 150 µM.

166 We determined the ATPase activity by measuring the P_i production rate (in µM min^{-1}) as a
167 function of His-MinD concentration. When we first tested His-MinD by itself at concentrations
168 between 0.5 µM and 16 µM, however, only baseline activity below the detection limit could
169 be observed (data not shown). Since MinD interacts with the membrane and it was expected
170 that the ATPase cycle is involved in controlling this interaction, we next measured ATPase
171 activity in the presence of liposomes extruded from *E. coli* total lipids (Avanti). Remarkably,
172 this led to a robust increase in ATPase activity of His-MinD, appearing to be linearly dependent
173 on protein concentration (Fig. 1 A & B). To be able to compare the activity level to the
174 published *E. coli* MinD *in vitro* ATPase data (63-65), the specific activity is expressed in nmol
175 mg^{-1} min^{-1} (Fig. 1 B). To our surprise, activity levels of recombinant *B. subtilis* MinD were found
176 to be on par with fully active *E. coli* MinD in conjunction with MinE and phospholipids (63).
177 Moreover, the ATPase activity did not show cooperative behavior compared to *E. coli* MinD at
178 lower concentrations (63). We further measured that ATP hydrolysis can be titrated with both
179 ATP and liposomes and is described by Michaelis-Menten kinetics (Fig. 1 C & D). Again, the

180 hereby-obtained V_{max} values (19.50 nmol mg^{-1} min^{-1} and 22.05 nmol mg^{-1} min^{-1}, respectively)

181 indicate similar MinD ATPase activity levels between both organisms.

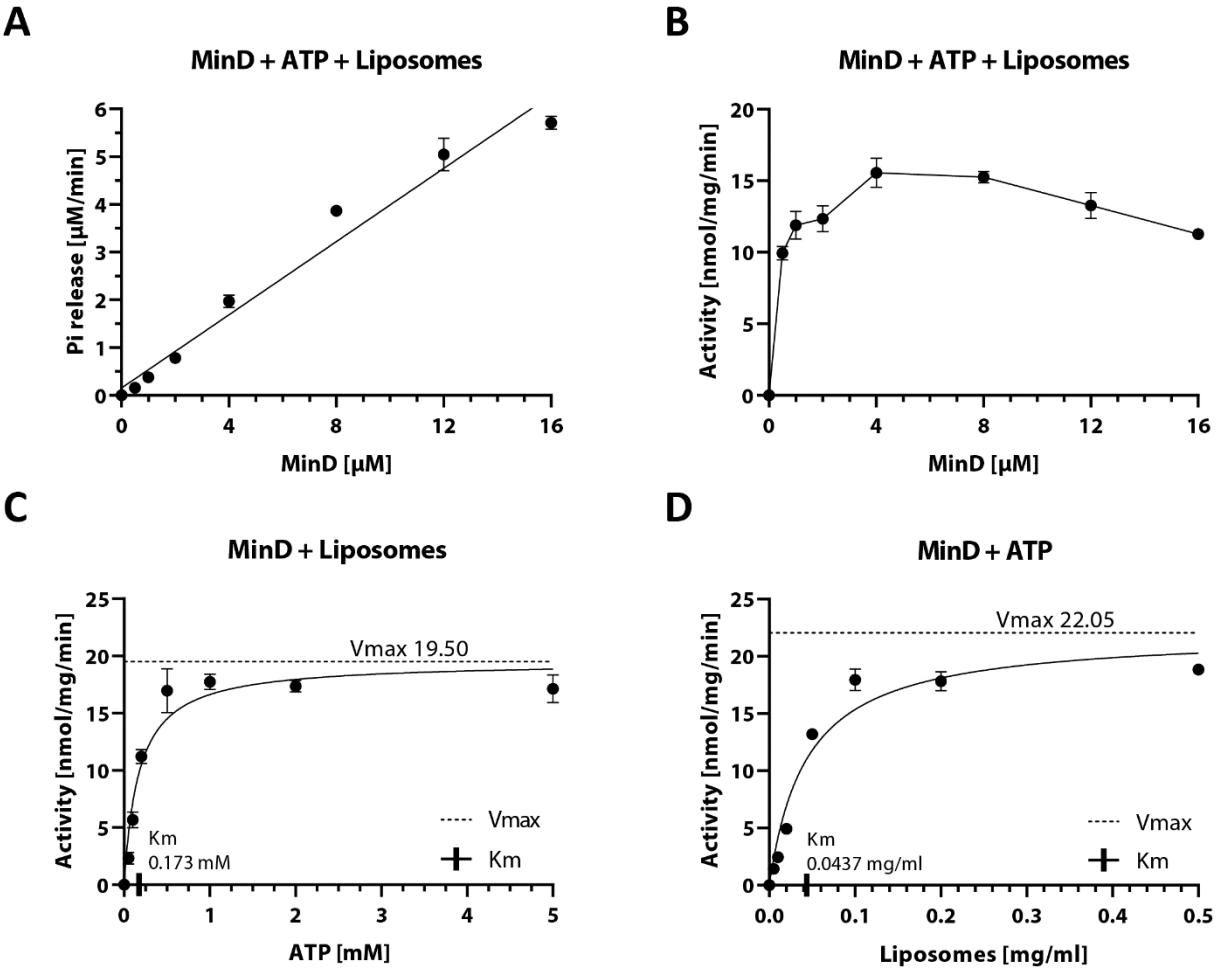

182

183 **Fig. 1: Biochemical analysis of *B. subtilis* MinD ATPase cycle.**

184 (A) Phosphate release plotted against different MinD concentrations, fitted with a simple
185 linear regression (R^2 = 0.97). Phosphate release was measured using the EnzChek™ phosphate
186 assay kit. Samples contained 0.2 mg ml^{-1} liposomes and were pre-incubated for 10 minutes
187 before addition of 2 mM Mg^{2+}-ATP; n ≥ 3.

188 (B) Specific activity of the MinD ATPase from (A) measured as a function of MinD
189 concentration.

190 (C) Specific activity of MinD measured as a function of ATP concentration, determined as in
191 (B) with fixed MinD concentration of 10 µM. Fitting the Michaelis–Menten equation (black
192 lines) gives k_{cat} = 36.27 h^{-1}, V_{max} = 19.50 nmol mg^{-1} min^{-1} and K_M = 0.173 mM.

193 (D) Specific activity of MinD measured as a function of liposome concentration, determined
194 as in (B) with fixed MinD concentration of 6 µM. Fitting the Michaelis–Menten equation (black
195 lines) gives k_{cat} = 41.01 h^{-1}, V_{max} = 22.05 nmol mg^{-1} min^{-1} and K_M = 0.0437 mg/ml.

196 **MinD ATPase activity is triggered by membrane binding**

197 To be able to test if membrane-interaction itself is the catalyst for MinD ATPase activity, the
198 need for a membrane-binding mutant was evident. MinD interacts with the membrane
199 through an amphipathic α-helix located at the N-terminus, thus being the membrane targeting
200 sequence (MTS) (Fig. 2 A). Exchanging the hydrophobic isoleucine residue in the apolar core
201 of the MTS with a charged glutamate (I260E) has been shown to abolish membrane binding
202 of MinD by perturbing the amphipathic properties, demonstrated through fluorescence
203 microscopy (66). Accordingly, a His-MinD-I260E variant was constructed and purified via the
204 established purification protocol. The yield of the purification was extensively higher
205 compared to the wild type protein (Fig. S 3), hinting towards a successful abolishment of
206 membrane interaction.

207 Moreover, as we wanted to be able to compare *in vivo* and *in vitro* data, a *B. subtilis* strain for
208 microscopy was constructed, where the native copy of MinD was replaced by a HaloTag-MinD
209 fusion protein (Fig. 2 B, HaloTag will henceforth be referred to as Halo). We then introduced
210 the I260E mutation, resulting in a strain producing Halo-MinD-I260E as the only copy.
211 Microscopic analysis of a Halo-MinD-I260E with TMR dye confirmed drastically reduced
212 membrane binding through its almost exclusive cytosolic localization (Fig. 2 B).

213 We next repeated ATPase activity assays with the purified, recombinant I260E mutant, and
214 remarkably, activity remained below the detection limit of the assay, while a positive control
215 of His-MinD wild type protein displayed regular activity (Fig. S 4). In summary, these data
216 collectively suggest that membrane binding is necessary and the key trigger for ATP hydrolysis
217 of *B. subtilis* MinD, without the apparent need for another stimulus.

218 This conclusion arose new questions that needed to be answered in order to understand the
219 ATPase cycle of MinD in *B. subtilis*. Membrane binding of MinD in *E. coli* is primarily possible
220 for the ATP bound, dimeric form, but if that were the case in *B. subtilis*, can dimers only form
221 in the cytosol? Alternatively, can *B. subtilis* MinD bind the membrane as monomers, so that
222 the membrane could act as a proxy for dimerisation of MinD?

223 **Construction of catalytic MinD mutants**

224 To be able to answer these questions, we explored further mutations that affect the ATP
225 binding region and thus the dimerization process. Due to the conserved nature of Walker-type
226 MinD/ParA-like ATPases, residues involved in catalytic activity have been well characterized
227 so that different ATPase mutants have been established (67-69). We therefore constructed
228 expression plasmids encoding three different MinD variants (illustrated in Fig. 2 A): This first
229 mutation, MinD-G12V, produces a steric clash within the active site, so that ATP can still be
230 bound, but dimers cannot form (67, 68). The second mutation, K16A, completely disrupts ATP
231 binding and hence yields another monomeric mutant (67). The third variant encodes the
232 mutation D40A, which should interfere with ATP hydrolysis (68, 69). Therefore, it was
233 expected that MinD-D40A forms a trapped nucleotide sandwich dimer similar to Soj or *E. coli*
234 MinD (68, 69). All MinD variants were successfully expressed and purified with the previously
235 established protocol and resulted in similar protein yields when compared to the wild type
236 protein (Fig. S 1, Fig. S 5, Fig. S 6 and Fig. S 7). When evaluating the gel filtration
237 chromatograms, His-MinD-G12V elute in a single peak, which can be interpreted as a
238 monomer when compared to the wild type His-MinD elution peak (Fig. S 2). His-MinD-D40A
239 on the other hand also eluted in a single peak, albeit being wider and eluting earlier, indicating
240 a mainly dimeric conformation. Only His-MinD-K16A reproducibly formed a rather unexpected
241 shoulder in its main elution peak, which could hint towards further interaction with the gel

242 filtration matrix or other potential self-interactions. As expected, all of the recombinant His-
243 MinD mutants were catalytically inactive when tested via the EnzChek phosphate assay kit.

244 To investigate *in vivo* effects of these variants, the same mutations were introduced into the
245 strain expressing Halo-MinD in *B. subtilis*, respectively, and subsequently imaged via wide-
246 field microscopy (Fig. 2 B). Surprisingly, both monomeric MinD variants (G12V and K16A) were
247 still observed to be membrane associated, however resulting in the apparent loss of the polar-
248 septal MinD gradient (Fig. 2 B). All strains producing MinD mutants manifested an increased
249 cell length and minicell production, as it was expected in cells containing dysfunctional Min
250 proteins. Finally, the locked dimer D40A mutant appeared to be mainly membrane associated,
251 thereby forming large foci indicating accumulation of MinD, but much less dispersed when
252 compared to G12V or K16A (Fig. 2 B). In summary, the time-resolved MinD gradient appears
253 to be lost in all MinD mutants, including D40A. This suggests that the ATPase cycle and thus
254 quick cycling of MinD is indeed necessary for formation of the observed dynamic gradient, as
255 it has been previously suggested (60).

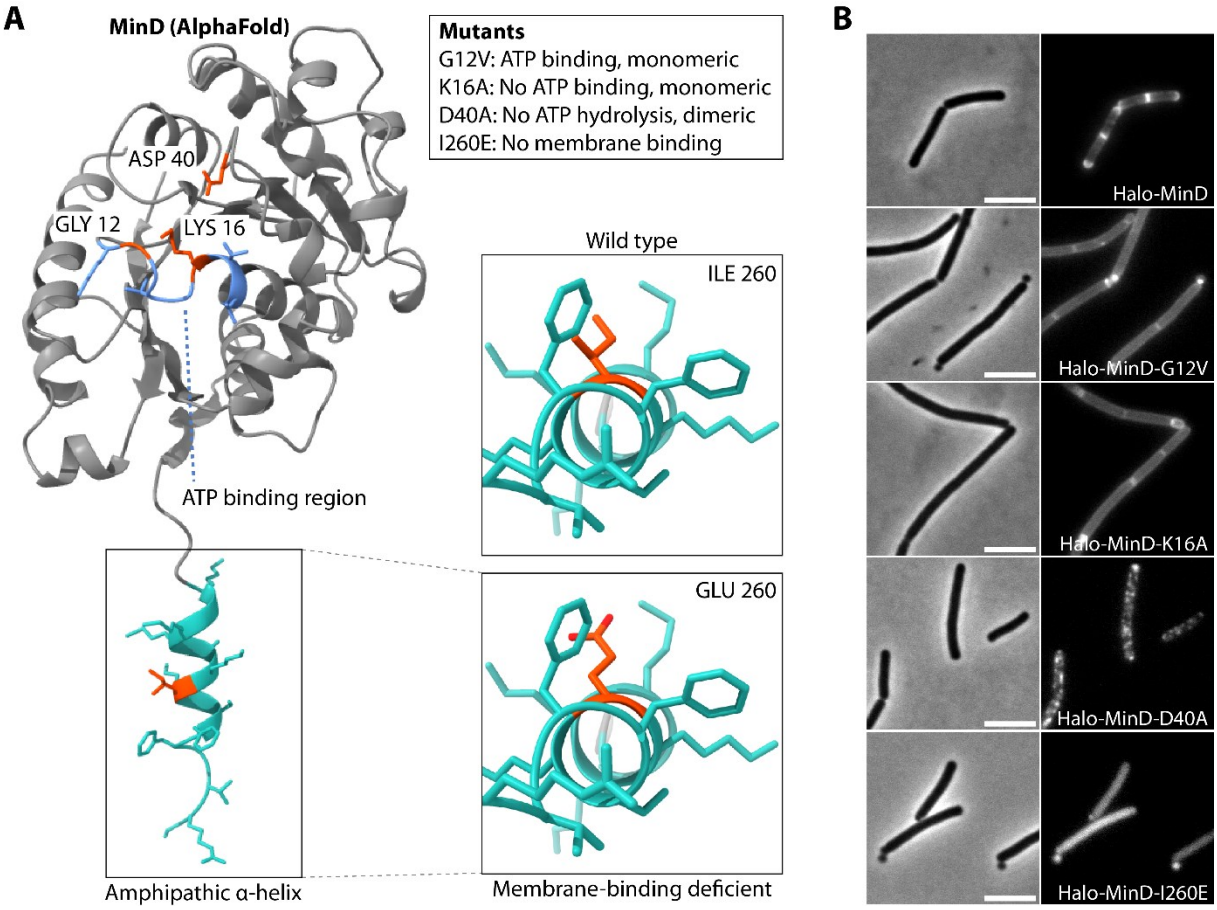

Fig. 2: Cartoon of MinD AlphaFold model with highlighted key amino acids and the effects of their mutagenesis.

(A) Left: Rendering of MinD AlphaFold model with ATP binding region highlighted in light blue, membrane targeting sequence (MTS) in turquoise and key residues in orange; Box: explanation of mutagenesis effects. Right: Close-up on hydrophobic region of amphipathic helix.

(B) Representative wide-field microscopy images of *B. subtilis* expressing indicated Halo-MinD variants as the only MinD copy from the native locus, stained with TMR ligand. Left: Phase contrast; scale bar 5 µm. Right: fluorescence.

266 **Monomeric MinD binds the membrane with high efficiency.**

267 Membrane binding appeared to be a key factor of the ATPase cycle and since the microscopy-
268 data indicated binding of MinD monomers to the membrane, we next aimed to determine
269 biochemically, if the respective MinD variants are capable of binding to membrane and if so,
270 to characterize their respective binding kinetics. To this end, we employed Bio-layer
271 interferometry (BLI), a technique capable of quantifying binding strength and protein
272 interaction, as well as identifying reaction kinetics.

273 As we were interested in MinD-membrane interaction, the first step was to immobilize
274 liposomes on a biosensor to create a membrane-like surface. Therefore, *E. coli* total lipids
275 (Avanti) were extruded after mixing in a ~33:1 ratio with DSPE-PEG$_{(2000)}$-biotin (Avanti), a
276 biotinylated polyethylene glycol lipid extending from the liposomes and able to bind
277 Streptavidin (SA) coated biosensors (70, 71). After successful saturation of the sensor with
278 liposomes, MinD-liposome association and dissociation could be measured, a scheme of the
279 experimental set-up is depictured in Fig. 3 A. As a negative control for unspecific binding,
280 MinD-sensor interaction was tested on empty SA sensors. Furthermore, unspecific binding to
281 liposome-saturated sensors was tested using bovine serum albumin (BSA). Both resulted in
282 negligible, diffuse signal (data not shown).

283 Kinetics of His-MinD binding were tested first, using different protein concentrations between
284 1 µM and 16 µM in presence of ATP. Binding to the sensor-bound liposomes scaled with
285 increasing protein concentration, resulting in an equilibrium dissociation constant K_D = 7.17
286 µM and an association rate constant k_{on} = 3.03 x 10^3 M^{-1} s^{-1} as a reference point for the wild
287 type protein (Fig. 3 B, Tab. 1). Unsurprisingly, His-MinD-I260E showed a more than 10-fold
288 reduced affinity to the membrane with a K_D = 74.36 µM (Tab. 1), which is also apparent in the

289 binding graph (Fig. 3 B). The strong increase in K_D is based on the over 16-fold lowered
290 association k_{on} = 0.18 x 10^3 M^{-1} s^{-1}, while the dissociation k_{off} = 13.45 x 10^{-3} s^{-1} was also slightly
291 lower when compared to wild type MinD. Next, both monomeric mutants G12V and K16A
292 were probed, and to our surprise, capable of membrane interaction (Fig. 3 C & D, Tab. 1). This
293 is in stark contrast to *E. coli* MinD, where dimerization needs to precede membrane binding
294 to achieve sufficient affinity (44, 45, 64, 69, 72). Similar to I260E, the G12V mutant displayed
295 an around 10-fold reduced membrane affinity equilibrium with K_D = 75.38 µM (Tab. 1).
296 However, G12V only exhibited a ~5 fold reduced binding affinity with k_{on} = 0.63 x 10^3 M^{-1} s^{-1}
297 when compared to the wild type MinD, while the k_{off} = 47.8 x 10^{-3} s^{-1} represents the fastest
298 dissociation rate constant between all MinD variants and more than 2-fold increase compared
299 to wild type MinD (Tab. 1). This indicates a higher turnover and thus a quicker release of the
300 protein from the membrane. Markedly different from this, K16A displayed a K_D of 1.36 µM,
301 but not much lower binding rates (k_{on} = 2.03 x 10^3 M^{-1} s^{-1}, Tab. 1 & Fig. 3 C). Instead, the low
302 K_D can be mostly attributed to the reduced dissociation (k_{off} = 2.77 x 10^{-3} s^{-1}), implying a much
303 longer retention of His-MinD-K16A at the membrane (Fig. 3 D). Since G12V can bind ATP while
304 K16A cannot, these findings reveal that presence of ATP in the binding pocket affects
305 association and dissociation of MinD.

306 Last, the His-MinD-D40A mutant protein was probed, resulting in an almost 10-fold reduced
307 dissociation equilibrium K_D = 0.74 µM (Tab. 1, Fig. 3 E). Here, the strongly reduced membrane
308 dissociation (k_{off} = 1.76 x 10^{-3} s^{-1}) causes the drastic change in K_D, which we expected for the
309 trapped dimer, as it could position the two amphipathic helices into a more optimal
310 orientation of the apolar residues towards the membrane, resulting in stronger binding and
311 no capability of hydrolyzing ATP and thus relieving the dimer (66, 68, 69).

312 In summary, these BLI data demonstrate that *B. subtilis* MinD is capable of binding membrane

313 in both monomeric and dimeric form, while the presence of ATP in the binding pocket appears

314 to affect both membrane binding and dissociation.

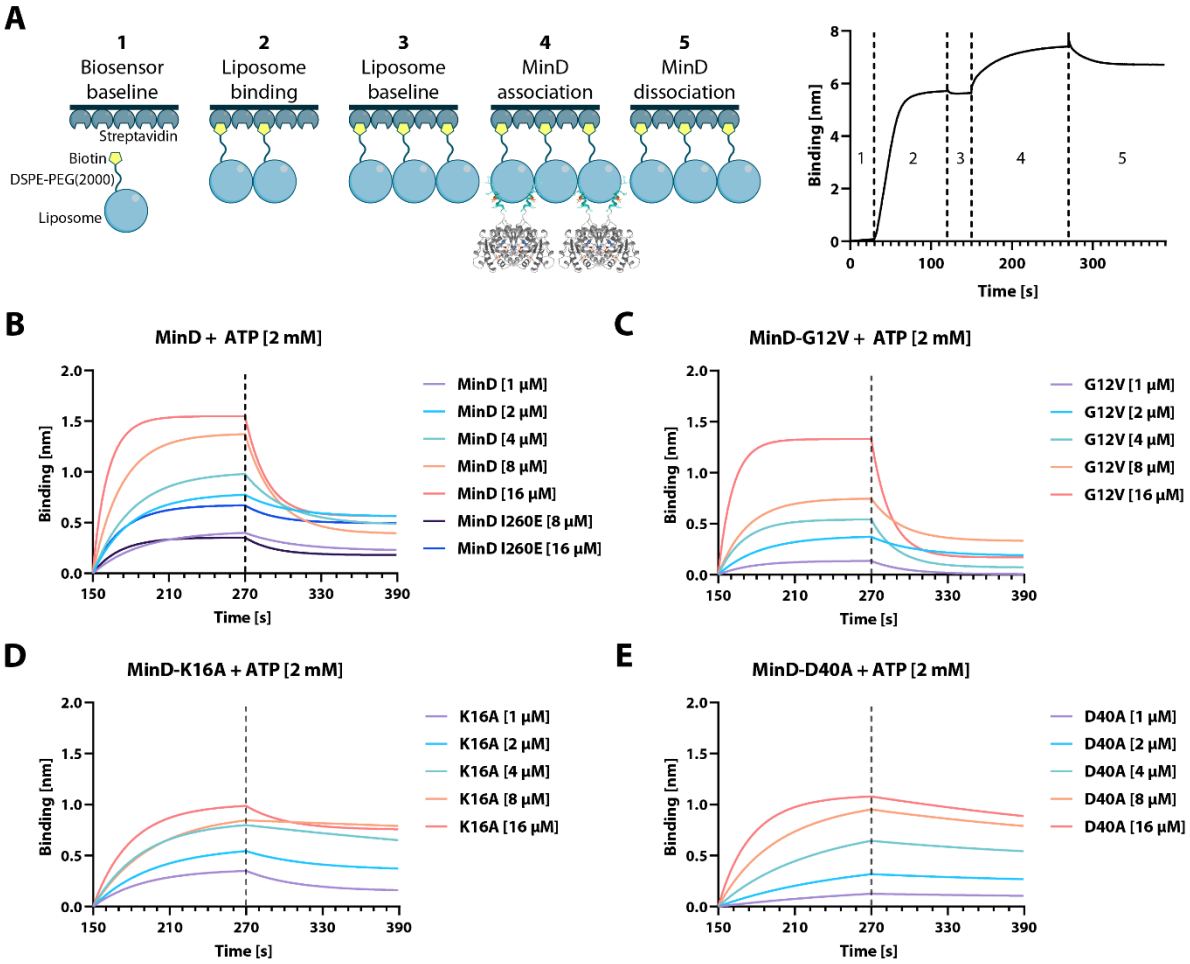

315

316 **Fig. 3: BLI analysis of His-MinD and different mutants.**

317 (A) Left: Cartoon representation of the different BLI steps, starting with (1) establishing a
318 baseline in protein buffer, (2) binding of liposomes through the biotinylated DSPE-PEG(2000)
319 phospholipid, (3) establishing a new baseline, (4) binding of MinD and finally (5) dissociation
320 of MinD. Right: Exemplary graph resulting from sensor readouts of steps (1) - (5). Scheme
321 adapted from (70).

322 (B) MinD binding plotted against time through association and dissociation phase (steps 4-5)
323 at different protein concentrations, including the His-MinD-I260E mutant.

324 (C) – (E) Same as (B) using the indicated respective mutant of His-MinD (G12V, K16A and
325 D40A).

326 **Tab. 1: Kinetic constants of His-MinD and variants obtained via BLI.**

Protein	K_D [µM]	k_{on} [M^{-1} s^{-1}]	$k_{on\ error}$	k_{off} [s^{-1}]	$k_{off\ error}$	X^2	R^2
MinD	7.17	3.03×10^3	0.13×10^3	21.7×10^{-3}	0.33×10^{-3}	16.07	0.95
MinD-G12V	75.38	0.63×10^3	0.19×10^3	47.8×10^{-3}	1.13×10^{-3}	13.89	0.95
MinD-K16A	1.36	2.03×10^3	0.062×10^3	2.77×10^{-3}	0.088×10^{-3}	6.966	0.95
MinD-D40A	0.74	2.39×10^3	0.053×10^3	1.76×10^{-3}	0.069×10^{-3}	6.006	0.98
MinD-I260E	74.36	0.18×10^3	0.19×10^3	13.45×10^{-3}	0.38×10^{-3}	3.607	0.95

327 K_D = equilibrium dissociation constant; k_{on} = association rate constant; k_{off} = dissociation rate constant

328 **Single-molecule localization microscopy confirms *in vitro* data.**

329 To validate our findings, which were based on biochemical *in vitro* results, we decided to utilize
330 single-molecule localization microscopy (SMLM) with focus on single-molecule tracking (SMT),
331 a technique allowing to observe and evaluate MinD dynamics *in vivo* inside living *B. subtilis*
332 cells. For this reason, the previously introduced strains expressing Halo-MinD and variants
333 (Tab. S 3), respectively, were grown to mid-exponential phase, stained with TMR and
334 subsequently transferred and imaged on agar pads supplemented with medium. Every field
335 of view (FOV) was imaged for 10,000 frames of 24 ms each, and individual fluorescence
336 localizations were either fitted with the Zen Black software (Zeiss) and analyzed with individual
337 R scripts for localization data (Fig. 4 A), or TrackMate and the SMTracker 2.0 software packages
338 to build protein trajectories and to analyze mobility and dynamics (Fig. 4 B-E) (73-76).

339 We began SMLM analysis by plotting a heat-map of the intracellular localization of all
340 individually recorded Halo-MinD molecules as well as the mutated variants, respectively, on
341 normalized cells (Fig. 4 A). This representation did not only provide a robust internal control
342 for the imaging and post-processing process for the well characterized localization of MinD,
343 but also reveals systemic differences in localization caused by the respective mutations. The
344 first obvious difference is the lower local enrichment of MinD at the cell center and poles when
345 carrying the G12V or K16A mutation (Fig. 4 A). Here, the membrane-bound MinD fraction
346 seems to be much more evenly distributed along the membrane, similar to what we observed

347 during wide-field microscopy (Fig. 2 B). This result does not only confirm the ability of MinD
348 monomers to bind the membrane (Fig. 3 C & D), but also fuels the speculation that MinJ might
349 be unable to recruit MinD in its monomeric form, so that polar and septal recruitment by MinJ
350 requires dimeric MinD. In combination with the information obtained from BLI results (Fig. 3),
351 this could mean that the membrane itself serves as proxy for MinD dimerisation and
352 subsequent recruitment, quickly followed by ATP hydrolysis and membrane detachment of
353 MinD. In contrast, but in agreement with wide-field imaging (Fig. 2 B), the Halo-MinD-D40A
354 mutant does appear to frequently form foci and larger local accumulations, with little protein
355 in the cytosolic fraction (Fig. 4 A). This, again, could be caused by local MinJ interaction and
356 recruitment in combination with the missing capability of membrane detachment or with
357 increased lateral MinD interactions (77). Finally, the I260E mutant appears evenly distributed
358 throughout the cell (Fig. 4 A), as it was expected.

359 Independently, all protein trajectories were subjected to a stationary localization analysis
360 (SLA) (Fig. 4 B). This was done by first grouping all trajectories into an either mobile or static
361 population by testing if the molecule left a circle with a diameter of 97 nm (equaling the pixel
362 size of the imaging setup) within at least five consecutive frames. Trajectories that were
363 classified as mobile were further sub-grouped into mixed and free trajectories, where only
364 free trajectories never presented a confinement event (73). In agreement with previous data,
365 the D40A mutant displayed the highest fraction of static tracks (Fig. 4 B), and by far the lowest
366 proportion of truly free trajectories (48.5 %). In contrast, more than 90% of Halo-MinD-I260E
367 molecules were classified as free with only few trajectories classifying as static (Fig. 4 B),
368 accentuating the absence of interaction with the membrane or other structures. When
369 comparing Halo-MinD to the monomeric mutants G12V and K16A, the number of static tracks
370 was visibly reduced in the mutants. Since both monomers are unable to dimerise, it is less

371 likely that they can form larger clusters, which we observed in a previous study (60).
372 Moreover, interaction with MinJ stabilizes MinD (60), and the possible abolishment of this
373 stabilization should also result in a mobilizing effect. Between both monomeric mutants, K16A
374 displayed a slightly larger number of static trajectories (Fig. 4 B), which is in alignment with
375 BLI data, where the K16A mutant dissociates much less effective from the membrane (Fig. 2 C
376 & D, Tab. 1).

377 Next, we wanted to learn about the average intracellular mobility of Halo-MinD in comparison
378 to the mutated variants, which prompted us to analyze the mean-squared displacement (MSD,
379 Fig. 4 C). In MSD analysis, the traveled distances of recorded trajectories are plotted against a
380 given time lag (Δt) as a function of Δt, here one imaging frame (24 ms), where the slope can
381 indicate the speed (78-80). As expected, the I260E mutant displayed the fastest average
382 mobility, since it does not bind the membrane effectively anymore (Fig. 4 C). In contrast, the
383 D40A mutant was the slowest recorded protein, indicated by the only mild incline (Fig. 4 C).
384 Since we expect most of the proteins' population to be membrane bound, and furthermore
385 observed larger foci that suggest cluster formation, this was expected. Halo-MinD wild type
386 protein appeared to be more mobile in comparison (Fig. 4 C), as it should exist in both
387 monomeric and dimeric conformation and either freely diffusive in the cytosol or interact with
388 the membrane. Last, the two monomeric mutants G12V and K16A displayed extremely similar
389 average speeds that were both faster than the wild type protein (Fig. 4 C). Since these MinD
390 variants cannot form dimers, general diffusion should be faster, as there should be no MinD
391 dimers or oligomers, and possibly no recruitment by MinJ.

392 If the underlying movement in MSD analysis can be described by simple Brownian motion, the
393 gradient of the curve is proportional to the diffusion coefficient *D* (80). We know, however,
394 that MinD interacts at least with MinC, MinJ, the membrane and itself, in combination with

395 the fact that bacterial cells exhibit natural confinement. With these information one cannot
396 assume simple Brownian motion, therefore we have chosen jump distance (JD) analysis as a
397 more in-depth assessment to describe Halo-MinD dynamics (Fig. 4 D & E). In JD analysis, the
398 distances molecules travel between subsequent frames are plotted in a probability
399 distribution (Fig. 4 E), and diffusion coefficients are obtained by curve fitting (80), in this case
400 with a three-component model separating fast, slow and confined molecules (Fig. 4 D & E). To
401 be able to compare population sizes better, the simultaneous option was chosen in the
402 SMTracker software, fixing the diffusion coefficients for every MinD variant (73). To also
403 obtain individual, variant specific diffusion coefficients, the same data was additionally fitted
404 individually (non-simultaneous SQD analysis in SMTracker2, Tab. 2).

405 Generally, the results of JD analysis correlated well with our *in vitro* data. When dissecting the
406 different populations in the wild type, more than a third of all proteins appear to be confined
407 (36.6%, Fig. 4 D), which likely comprises membrane bound protein that is further stabilized by
408 protein-protein interactions via lateral interaction of MinD with MinC and MinJ. The slow
409 mobile population was the largest (45.7%, Fig. 4 D), and possibly summarizes different
410 conformations of MinD that interact with the membrane, but are still diffusive and not
411 captured or stabilized through further interactions. The third, fast diffusive population (17.7%,
412 Fig. 4 D) likely recapitulates cytosolic MinD. These results stress the importance of the MinD
413 ATPase cycle for its localization and dynamics, as these are severely altered in the MinD
414 mutants.

415 In detail, the probability distributions of Halo-MinD-D40A and I260E (Fig. 4 E) illustrate the
416 strong shift between MinD molecules in a confined (D40A) and a diffusive state (I260E) best.
417 When examining the different populations, most Halo-MinD-D40A molecules were classified
418 as confined (54.2%) and slow mobile (40.2%), whereas I260E only displayed ~9% of confined

419 molecules (Fig. 4 D), matching prior results and expectations of the membrane binding
420 mutant. When comparing D40A to wild type Halo-MinD, the largest shift is observed between
421 the fast mobile and confined populations, shifting towards a distinctively more confined
422 regiment in the D40A mutant (36.6% WT, 52.2% D40A; Fig. 4 D) and visible disappearance of
423 the fast population in the probability distribution (Fig. 4 E). These results are in line with the
424 previous observations, as a trapped dimer of MinD will remain at the membrane at much
425 higher efficiency (Fig. 3 E & Tab. 1), and appeared to form foci and clusters (Fig. 2 B, Fig. 4 A),
426 with the possibility of stabilization through MinJ. G12V and K16A mutants on the other hand
427 showed an increase in fast mobile populations (WT 17.7%, G12V 25.8%, K16A 26.6%; Fig. 4 D
428 E), which could be attributed to a reduced interaction with MinD interaction partners (MinC,
429 MinJ and plasma membrane). This notion is supported by the decrease in confined molecules
430 for both G12V and K16A mutants compared to the wild type (WT 36.6%, G12V 23.7%, K16A
431 29%; Fig. 4 D & E), which are expected to be membrane bound and likely stabilized through
432 other protein-protein interaction, which may be reduced or absent in the monomeric
433 conformation. Finally, when comparing both monomeric variants, the K16A mutant displays a
434 noticeable shift between the slow diffusive (G12V 50.5%, K16A 44.3%; Fig. 4 D) and confined
435 populations (23.7% G12V, 29% K16A; Fig. 4 D). The larger confined population of Halo-MinD-
436 K16A is consistent with the BLI results (Fig. 3 D, Tab. 1), where K16A appears to have a lower
437 dissociation from the membrane, increasing its likelihood of confinement, possibly caused by
438 the inability to bind ATP.

439 In summary, these results emphasize the importance of the MinD ATPase cycle for
440 functionality of the Min system in *B. subtilis*. Even though *B. subtilis* MinD is not capable of
441 oscillation, its intracellular dynamics are highly dependent on the functionality of the MinD
442 ATPase domain and its catalytic site, which is reflected by the variety of localization and

interaction defects displayed by the MinD mutants on a molecular level, that all result in severe division anomalies.

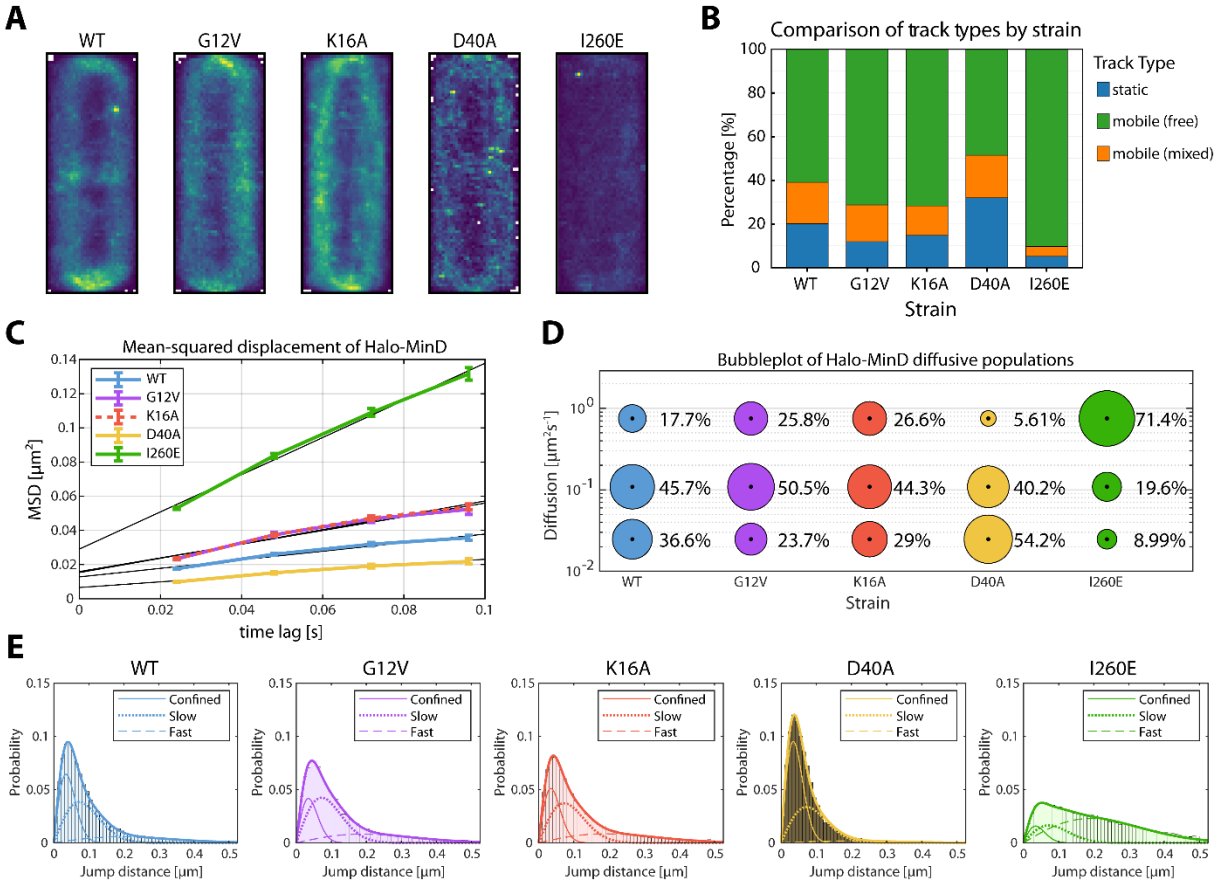

Fig. 4: Single-molecule localization microscopy analysis of Halo-MinD and mutants expressed in *B. subtilis*.

Exponentially growing *B. subtilis* cells expressing Halo-MinD and variants (n ≥ 48 cells, respectively) were stained with TMR ligand and subsequently imaged. Individual protein trajectories were recorded using SMLM and analyzed with Zen blue (Zeiss), Trackmate, the SMTracker 2.0 software package and manual scripts in R. Minimum track-length 4 frames of 24 ms, with at least 2596 trajectories per strain.

(A) Heat map representation of intracellular localization of individual molecules of Halo-MinD and variants, respectively, plotted on normalized cells. Brighter colors indicate higher abundance.

(B) Barplot of stationary localization analysis (SLA), comparing different track types within the protein population. Tracks were considered static when not leaving a circular area of 97 nm diameter within 5+ frames. Mobile populations were further divided into free and mixed tracks, where mixed tracks displayed a switch between free and confined movement.

460 (C) Plot of the mean-squared displacement of Halo-MinD and variants over time, fitted with a
461 linear fit excluding the last timelag.

462 (D) Bubble plot displaying single-molecule diffusion rates of the indicated MinD fusions.
463 Populations were determined by fitting the probability distributions of the frame-to-frame
464 displacement (jump distance) data of all respective tracks to a three components model (fast
465 mobile, slow mobile and confined protein populations).

466 (E) Probability distributions of jump distances of Halo-MinD and variants. Data was fit with a
467 three component model, indicating confined, slow and fast tracks.

468

469

470 **Tab. 2: Diffusion coefficients obtained from non-comparative SQD analysis of Halo-MinD**
471 **and variants fitted with three populations.**

Strain	Fast diffusive [$\mu m^2 s^{-1}$]	Slow diffusive [$\mu m^2 s^{-1}$]	Confined [$\mu m^2 s^{-1}$]
MinD WT	0.60 (22.3 %)	0.084 (50.4 %)	0.020 (27.3 %)
MinD-G12V	0.68 (28.5 %)	0.10 (47.5 %)	0.026 (24.0 %)
MinD-K16A	0.70 (27.3 %)	0.11 (43.9 %)	0.024 (28.8 %)
MinD-D40A	0.44 (13.7 %)	0.063 (50.0 %)	0.021 (36.3 %)
MinD-I260E	0.76 (73.4 %)	0.095 (20.3 %)	0.022 (6.3 %)

472 Percentages indicate relative population size

473

474 ## Discussion
475

476 Pattern formation is a universal trait of living cells and tissues and a crucial factor in cellular
477 self-organization (81). This is best exemplified during embryonic development, where
478 eukaryotic cells differentiate into various types that form specific tissues and organs. In
479 particular, the formation of the body axis and the segmentation of the fruit fly embryo is
480 governed by specific patterns that dictate the development of different body parts (82, 83).
481 Disruptions in pattern formation leads to developmental abnormalities and diseases. Bacteria
482 are single celled organisms, however, their morphogenesis also depends on subcellular
483 pattern formation of morphogenic proteins that ensure correct synthesis of the cell
484 components. These self-organizational process have been explained by the reaction-diffusion
485 theory, first proposed by Alan Turing (84). The beauty of the reaction-diffusion theory is that
486 it can explain complex spatio-temporal organizations even in absence of a preexisting
487 asymmetry. Thus, symmetry breaking is a key aspect of *de novo* pattern formation (85). The
488 model of the reaction diffusion theory is simply based on two components, an activator and
489 an inhibitor, that interact chemically and diffuse at different rates in a given medium, such as
490 the cytoplasm of a cell. Pattern formation is generated if one of the components diffuses
491 differently to the other. Depending on the precise nature of the interaction and the diffusion
492 properties, a variety of stable patterns can be generated by this process. In bacteria, the
493 oscillation of MinCDE in *E. coli* is one of the finest examples of such a reaction-diffusion
494 system, and the two core components MinD and MinE cycle between membrane and cytosol
495 in an ATP-dependent manner, generating a standing wave with a time-resolved minimum at
496 midcell (15, 86). Here, binding and unbinding of the components to the membrane surface
497 influences the diffusion coefficients and controls the activation/inactivation of the cell division

498 inhibitor MinC (87). The mechanism and dynamics of the *E. coli* MinCDE system have been
499 subject of numerous studies and the system is therefore one of the best understood examples
500 of intracellular pattern formation in bacteria (15, 87-89). In comparison, the dynamics of the
501 Min system in *B. subtilis* have not been as well characterized. In this system, the activator of
502 MinD ATP hydrolysis, MinE, is missing and therefore the MinD dynamics remained
503 mechanistically unsolved. In a previous work we have characterized the subcellular dynamics
504 of Min components in *B. subtilis* using FRAP analysis (60). Although the scaffold protein DivIVA
505 was long considered a static interaction hub at the cell poles and at growing septa, our data
506 revealed that DivIVA is dynamically relocating within the cell, mainly associated in clusters at
507 the cell membrane (58-60). Cluster formation was also observed for MinJ and MinD, with a
508 clear enrichment of these clusters at the sites of septation. The observed dynamics explained
509 how the entire Min system including DivIVA, MinJ, MinD and MinC quickly re-localizes from
510 cell poles to midcell at the onset of cell division. Using the measured diffusion coefficients for
511 the Min proteins in combination with their native protein numbers, a mathematical model
512 was generated that suggested MinD protein gradient formation by a nonequilibrium process
513 (60). We suggested that gradient formation depends on the ATPase driven MinD dynamics.
514 However, in spite of a lack in biochemical data, we had to assume that the *B. subtilis* MinD
515 cycles between membrane-bound and cytosolic localizations, based on ATP-binding and
516 hydrolysis, similar to the situation that is well established for the *E. coli* MinD (60). A further
517 gap in our knowledge of the *B. subtilis* Min system concerns the activation mechanism of the
518 MinD ATPase in the absence of a MinE homolog. To fill this gap, we started to analyze the *B.*
519 *subtilis* MinD protein biochemically *in vitro*. The isolated MinD protein revealed a basal ATPase
520 activity that was stimulated by addition of liposomes (membrane). The *E. coli* MinD also
521 requires lipid addition to stimulate ATPase activity, however, it also requires addition of the

522 MinE protein for stimulation (63). The maximum activity for the *E. coli* MinD was determined
523 to be around 20 nmol mg^{-1} min^{-1} at conditions of full stimulation in presence of MinE and lipid
524 (63, 64). Surprisingly, the maximal activity of the *B. subtilis* MinD was almost precisely at the
525 same velocity, indicating that *B. subtilis* MinD ATPase activity is triggered by membrane
526 binding and may not require an additional protein factor such as MinE for its catalytic
527 activation. When comparing to other MinD/ParA ATPases that have been biochemically
528 characterized, the activity level of *B subtilis* MinD is on the lower end of the spectrum with a
529 measured k_{cat} of 36.27 h^{-1}. Soj, the ParA homologue in *B. subtilis*, reaches more than 2-fold
530 higher catalytic activity (83.6 h^{-1}) when fully activated by supplementing Spo0J (ParB) and DNA
531 (90), similarly to Soj in *Thermus thermophiles* combined with Spo0J and *parS* containing DNA
532 (68). Studies investigating the activity levels of ParA in *Caulobacter crescentus*, purified in
533 presence of ATP, determined a k_{cat} of 0.79 min^{-1} (47.4 h^{-1}) in absence of ParB, increasing almost
534 5-fold to 3.7 min^{-1} (222 h^{-1}) in presence of ParB (91). A more recent study found the *C.*
535 *crescentus* ParA k_{cat} increase from 5.8 hr^{-1} to 120 hr^{-1} upon addition of ParB (92).

536 Thus, it is very plausible that the *B. subtilis* MinD does not need an additional protein partner
537 that induces ATP hydrolysis. Rather, binding of MinD to the membrane itself is sufficient to
538 stimulate ATP hydrolysis. While we cannot entirely rule out the possibility that interactions
539 such as MinD binding to MinJ might further enhance nucleotide hydrolysis, the comparison of
540 maximum velocities, activity stimulation factors, and K_M values between the *E. coli* and *B.*
541 *subtilis* MinD proteins suggests that a functional homolog of the MinE protein is not necessary
542 in *B. subtilis*. MinD was shown to form larger complexes at the membrane, or, in case of the
543 *E. coli* protein co-polymers with MinC. However, the observed ATPase activities follow
544 Michaelis-Menten kinetic and are not cooperative, indicating that the MinD dimer is the active
545 component.

546 With the goal of testing binding of isolated MinD to the membrane, we designed a Bio-layer
547 interferometry experiment in which we immobilized liposomes and measured binding of
548 purified MinD proteins. Importantly, without addition of ATP (and ADP present from
549 purification) we observed only very week MinD binding to the liposomes (Fig. S 8), indicating
550 that MinD membrane binding and dissociation is coupled to the ATP hydrolysis cycle. In
551 presence of ATP, MinD readily binds to the liposomes with high affinity. Members of the
552 ParA/MinD protein family have been extensively studied and a set of mutations is well
553 characterized that allows generation of strictly monomeric MinD (G12V and K16A), a strictly
554 dimeric MinD variant (D40A) and a membrane binding mutant (I260E) (66-68). The most
555 intriguing observation of the binding experiments is that MinD monomers can apparently bind
556 to the liposome membrane in vitro. Both monomeric mutants (G12V and K16A) are readily
557 binding to the membrane, but the release of the proteins from the membrane surface differs
558 drastically. While the K16A mutant, unable to bind ATP, has a slow membrane release rate
559 (k_{off} rate of only $2.77*10^{-3}$ s^{-1}), the G12V monomeric mutant, which can still bind ATP, is
560 released fast from the membrane (k_{off} rate $47.8*10^{-3}$ s^{-1}). The D40A mutant of MinD, which is
561 thought to be a stable ATP-bound dimer, releases also with very slow kinetics (k_{off} rate
562 $1.76*10^{-3}$ s^{-1}), indicating that ATP hydrolysis is accelerating release of the MinD proteins from
563 the membrane and that ATP binding itself seems to affect association and dissociation
564 dynamics of MinD. These findings crucially support a reaction diffusion model in which the
565 MinD ATPase hydrolysis cycle is essential for pattern formation of *B. subtilis* MinD. It would
566 have been desirable to study the interaction of MinD with reconstituted MinJ proteins to
567 investigate the influence that MinJ has on membrane interaction of MinD. Unfortunately, we
568 did not succeed in the purification of a full length MinJ protein so far. MinJ contains seven
569 predicted transmembrane helices rendering isolation difficult. Also, the protein was prone to

570 degradation. However, a MinJ mediated stabilization of MinD at the membrane would be
571 comparable to the stabilizing effect that MinE has on MinD oligomers in *E. coli* (93, 94), and
572 was previously observed in our *in vivo* FRAP studies (60).

573 To get an idea of the MinD membrane interaction under *in vivo* conditions, we therefore
574 turned to state-of-the-art single molecule microscopy (SMLM) (95, 96). We expressed MinD
575 and all MinD point mutants as HaloTag fusions from their native locus in the min operon (allelic
576 replacement), similar to our previous work (60). This ensures native copy number regulation
577 and is a difference to most other studies on Min protein localization and dynamics in *E. coli* or
578 *B. subtilis*.

579 The locked MinD dimers (D40A mutant) frequently nucleated into larger membrane clusters.
580 This cluster formation is underlined by the drastic increase of the confined/immobile
581 population (54.2%) of D40A in SMLM. This increase in the static population comes to the
582 expense of freely diffusive protein, indicating that the vast majority of MinD D40A is
583 membrane associated. We observed a clear enrichment of these MinD clusters at the cell
584 poles and septa, lending support to the notion that MinD dimers are stabilized/recruited by
585 MinJ. This interpretation is supported by previous data showing that in absence of MinJ, MinD
586 proteins are randomly localized along the membrane in cluster, but not enriched at poles or
587 (in a *minJ* mutant background rare) septa (56). In line with this idea, the monomeric MinD
588 variants (G12V, K16A) are randomly bound to the membrane surface along the entire cell
589 length. The fact that we find most monomeric MinD proteins under the *in vivo* conditions
590 membrane associated also supports our *in vitro* measurements that MinD can bind in its
591 monomeric form to the membrane in *B. subtilis*. The time-resolved MinD gradient is lost in all
592 mutants, including D40A which should still be recruited by MinJ, suggesting the ATPase cycle
593 and thus MinD cycling is indeed necessary for proper formation of a gradient, as suggested

594 before (60). Our data are in perfect agreement with recent *in vitro* data collected with the *E.*
595 *coli* MinD using mass-sensitive particle tracking (MSPT) (77). MSPT analysis revealed that the
596 *E. coli* MinD forms lateral interactions, leading to higher order oligomers (trimer, tetramer and
597 even higher oligomers). It was speculated that dimerization of *E. coli* MinD at the membrane
598 leads to conformational changes opening an additional interaction surface of MinD for lateral
599 interaction (77). These lateral MinD interactions were thought to recruit further monomeric
600 MinD from solution to the membrane, thereby forming a nucleation for larger clusters. The
601 MinD cluster formation that we observed in *B. subtilis* using SMLM (60) are likely *in vivo*
602 evidence for this cooperative membrane binding. It should be noted that the MSPT analysis
603 was not sensitive enough to detect monomer binding to the membrane, but this was explicitly
604 not ruled out (77). Addition of a second amphipathic helix to the *E. coli* MinD however, was
605 shown to promote monomer binding of *E. coli* MinD to the membrane (65). Thus, the
606 difference between the *E. coli* and *B. subtilis* MinD is likely the higher membrane binding
607 capacity of the *Bacillus* protein. The observed cooperativity in membrane binding and thus
608 nucleation, as shown for the *E. coli* MinD in vitro (65, 77) and here for the *B. subtilis* MinD *in*
609 *vitro* and *in vivo*, is required for pattern formation by conferring nonlinearity (60, 97, 98).

610 In line with these ideas, our SMT data revealed that MinD proteins are found predominantly
611 in three populations with distinct diffusion coefficients. The MinD I260A mutant, impaired in
612 membrane binding, has a largely increased dynamic population, representing the freely
613 diffusive proteins in the cytoplasm. Therefore, we can assign the fastest population of the
614 other MinD variants, including the MinD wild type, with the diffusive, cytosolic fraction and
615 the slower mobile fraction with membrane associated proteins. The confined fraction is
616 therefore likely representing proteins that are either part of larger clusters or interact with
617 other proteins, thereby reducing the dynamicity. Furthermore, this likely indicates that all

618 MinD proteins in a cluster contribute to membrane binding. The two monomeric MinD
619 mutants have a reduced confined fraction in SMT analysis. This global comparison is also
620 supported by a detailed look into the diffusion coefficients of all MinD variants. These variant
621 specific diffusion coefficients can be obtained by analyzing the data shown in Fig. 4 individually
622 (non-simultaneous SQD analysis in SMTracker2 (Tab. 2). For the D40A mutant all three
623 populations: membrane associated cluster (D=0.021 µm^2 s^{-1}), membrane bound (D=0.063 µm^2
624 s^{-1}) and cytoplasmic diffusible populations (D = 0.44 µm^2 s^{-1}) display decreased diffusion
625 coefficients compared to wild type (and monomeric MinD variants). The freely diffusible and
626 the membrane associated wild type MinD protein are significantly faster (D=0.6 µm^2 s^{-1} and
627 D=0.084 µm^2 s^{-1}, respectively). The stable monomeric MinD variants (K16A and G12V) display
628 consistently higher diffusion coefficients, as expected. These data strongly argue for a
629 cytoplasmic pool of MinD proteins that can attach and release from the membrane surface in
630 an ATP depended fashion.

631 Thus, we conclude that membrane bound MinD dimers have a much stronger tendency to
632 interact with and recruit binding partners (including self-nucleation). This assumption is in
633 good agreement with findings of a recent report that analyzed MinD dynamics *in vivo* using
634 diffraction limited microscopy (99). In this study, a MinD D40A mutant hyper-recruited MinC,
635 leading to cluster formation of MinCD at the membrane. Deletion of MinC restored the MinD
636 gradient formation, indicating that MinC might indeed be part of a MinC/MinD co-polymer, as
637 suggested for the *E. coli* system (100).

638 Collectively, our data reveal that the MinD ATPase cycle is essential for regulated membrane
639 binding and release, which is crucial for the formation of a sharp MinD gradient at the septum
640 (60). However, in contrast to *E. coli* MinD, monomeric *B. subtilis* MinD can bind the membrane
641 with higher affinity, suggesting that MinD also dimerizes at the membrane surface. Dimer

642 formation is essential for ATPase activity, as indicated by our in vitro measurements, and is
643 necessary for efficient membrane detachment. The main characteristics of the *E. coli* MinD
644 with respect to membrane binding, self-interaction leading to nucleation, and membrane
645 detachment are therefore shared in the *B. subtilis* protein. These are the essential
646 requirements for Turing pattern formation by reaction diffusion. The difference, that ATP
647 hydrolysis of the *B*. *subtilis* MinD does not require a trigger other than membrane binding,
648 makes sense in a system that does not need to oscillate, but rather accumulate and sustain a
649 sharp gradient at the current site of division.

650

651 # Materials and Methods
652

653 **Bacterial strains, plasmids and oligonucleotides**

654 Plasmid and strain construction of all relevant constructs is described in the supplementary
655 information. Oligonucleotides, plasmids and strains used in this study are listed in Tab. S 1,
656 Tab. S 2 and Tab. S 3, respectively.

657 **Media and growth conditions**

658 *E. coli* was grown on lysogeny broth (LB) agar plates containing 10 g L^{-1} tryptone, 5 g L^{-1} yeast
659 extract, 10 g L^{-1} NaCl and 1.5% (w/v) agar at 37°C overnight using appropriate selection
660 (kanamycin 50 µg ml^{-1}, chloramphenicol 35 µg ml^{-1}).

661 *B. subtilis* was grown on nutrient agar plates using commercial nutrient broth and 1.5% (w/v)
662 agar at 37°C overnight. To reduce inhibitory effects, antibiotics were only used for
663 transformations and when indicated, since allelic replacement is stable after integration
664 (kanamycin 5 µg ml^{-1}, spectinomycin 100 µg ml^{-1}).

665 For microscopy, *B. subtilis* was inoculated to an OD_{600} 0.05 from a fresh overnight culture and
666 grown in MD medium - a modified version of Spizizen Minimal Medium (101) – at 37°C with
667 aeration in baffled shaking flasks (200 rpm) to OD_{600} 0.5-0.8. MD medium contains 10.7 mg
668 ml^{-1} K_2HPO_4, 6 mg ml^{-1} KH_2PO_4, 1 mg ml^{-1} Na_3 citrate, 20 mg ml^{-1} glucose, 50 µg ml^{-1} L-
669 tryptophan, 11 µg ml^{-1} ferric ammonium citrate, 2.5 mg ml^{-1} L-aspartate and 0.36 mg ml^{-1}
670 $MgSO_4$ and was always supplemented with 1 mg ml^{-1} casamino acids. Subsequently, cultures
671 were diluted to OD_{600} 0.05 in fresh, pre-warmed MD medium and grown to OD_{600} 0.5
672 (exponential phase).

673 **Purification of His-MinD and variants**

674 For heterologous expression of His-MinD and its variants, freshly transformed
675 BL21(DE3)/pLysS cells carrying the respective pET-28a expression vector (Tab. S 2) were
676 transferred to LB medium with appropriate selection (kanamycin 50 µg ml^{-1}, chloramphenicol
677 35 µg ml^{-1}) and grown overnight (37°C, 200 rpm). The next day, fresh LB was inoculated from
678 the overnight culture 1:150 and grown to OD_{600} 0.5 (37°C, 200 rpm) before IPTG (1 mM) was
679 added to induce His-MinD expression. Cells were harvested after 3 h, collected via
680 centrifugation (4°C, 5000 x g for 15 min) and stored at -80°C. For purification, a protocol of *E.*
681 *coli* MinD purification was adapted from (62): the cell pellet was resuspended on ice in lysis
682 buffer (50 mM NaH_2PO_4, 500 mM NaCl and 10 mM imidazole; pH 8.0), supplemented with
683 protease inhibitor cocktail (Roche), 0.2 mM Mg^{2+}-ADP and ~250 U mL^{-1} DNase I (Roche), and
684 subsequently lysed in a pre-cooled (4°C) French pressure cell (Amico; 3 x 1,200 psi). The debris
685 was then removed via centrifugation (10,000 g, 30 min, 4°C) and the supernatant was passed
686 through a 1 ml Ni-NTA column (Protino, Macherey-Nagel) utilizing liquid chromatography
687 (ÄKTApurifier). Here, the resin was washed with 10 ml binding buffer A (50 mM NaH_2PO_4, 500
688 mM NaCl, 20 mM imidazol; pH 8) before elution buffer B (50 mM NaH_2PO_4, 500 mM NaCl, 250
689 mM imidazol; pH 8) was added sequentially at concentrations of 5% (10 ml) 10% (20 ml), and
690 finally 100% (10 ml). His-MinD eluate was collected in 0.5 ml fractions. Fractions containing
691 high concentrations of protein (determined by chromatogram analysis, sodium dodecyl-
692 sulfate polyacrylamide gel electrophoresis (SDS-PAGE) and Western blotting using Penta-His
693 antibody (QIAGEN)) were pooled and concentrated using Amicon filter devices with 10 kDa
694 molecular weight cut-off (Millipore; Merck). Additionally, protein aggregates were removed
695 by pelleting them through centrifugation (10,000 g, 10 min, 4°C).

696 Next, the sample was purified using size-exclusion chromatography in gel filtration buffer C
697 (50 mM HEPES-KOH, 150 mM KCl, 10% (v/v) glycerol, 0.1 mM EDTA, supplemented with 0.4
698 mM TCEP and 0.2 mM Mg^{2+}-ADP just before use; pH 7.2) through a Superdex200 Increase
699 10/300 GL column (Cytiva) at a flow rate of 0.75 ml min^{-1}. Fractions containing His-MinD were
700 pooled and either directly used for the respective assays or stored at 4°C for a maximum of
701 one week. Final protein concentration was determined using Bradford assay with bovine
702 serum albumin (BSA) as standards. Protein purity and stability was confirmed via SDS-PAGE
703 using 12% polyacrylamide gels and Western blotting using Penta-His antibody (QIAGEN) (Fig.
704 S 1, Fig. S 5, Fig. S 6, Fig. S 7 and Fig. S 3).

705 **ATP hydrolysis assays**

706 ATP hydrolysis was analyzed in continuous reactions using the EnzChek Phosphate Assay Kit
707 (Thermo Fisher Scientific), according to the manufacturer's manual. Reaction volumes were
708 reduced to 100 µl and assayed in flatbottom 96-well plates (Greiner-UV-Star 96-well plates).
709 Reactions were measured at 37 °C continuously every minute over a time-course of 3 h in a
710 Tecan Infinite 200 Pro with the Software Tecan i-control v.2.0. If not indicated differently, the
711 reactions contained either 0-16 µM His-MinD or the respective variant as well as 2 mM Mg^{2+}-
712 ATP and 0.2 mg ml^{-1} liposomes. Liposomes were made from *E. coli* total extract (Avanti) by
713 first drying and then resuspending and rehydrating lipids in gel filtration buffer C (50 mM
714 HEPES-KOH, 150 mM KCl, 10% (v/v) glycerol, 0.1 mM EDTA). Next, the lipids were extruded 40
715 times through 100 nm polycarbonate membranes (Nuclepore™ Track-Etched Membrane 0.1
716 µm, Whatman). Before starting the reactions with 2 mM Mg-ATP, the plate was preincubated
717 for 10 min in order to eliminate phosphate contamination.

718 Data were first analyzed with Excel (normalized, subtraction of ATP auto hydrolysis and
719 subtraction of no substrate control), a linear regression was used to determine the hydrolysis
720 rate per minute. Data visualization and further analysis was performed using GraphPad Prism
721 version 9.4.0 for Windows, (GraphPad Software).

722 **AlphaFold prediction and structure-based analysis**

723 A structural model of *B. subtilis* MinD was calculated using AlphaFold2 (102) installed on a
724 local computer (Fig. 2 A), where the structural homology search was performed against the
725 full AlphaFold database as of 11.02.2024 (102).

726 **Bio-layer Interferometry**

727 Measurements were performed on the BLItz platform (Sartorius) using Streptavidin (SA)
728 Biosensors (Sartorius, 18-5019). The BLItz device was operated with the Software BLItz Pro
729 (version 1.3.1.3) using the advanced kinetics protocol modified as shown in Table S5 and
730 essentially as described before (103). Beforehand, Liposomes were made from a 33:1 mixture
731 of *E. coli* total extract (Avanti) and DSPE-PEG$_{(2000)}$-biotin (Avanti) by first drying and then
732 resuspending and rehydrating lipids in gel filtration buffer C (50 mM HEPES-KOH, 150 mM KCl,
733 10% (v/v) glycerol, 0.1 mM EDTA). Next, the lipids were extruded 40 times through 100 nm
734 polycarbonate membranes (Nuclepore™ Track-Etched Membrane 0.1 µm, Whatman).
735 Biosensors were hydrated for at least 10 min in a 96-well plate in 200 µl gel filtration buffer C.

736 As a starting point, unspecific binding was tested. For this, non-biotinylated His-MinD was
737 used to be loaded onto the Streptavidin biosensor. For the binding assays, all measurements
738 were performed in black reaction tubes with 200 µl gel filtration buffer C or the indicated
739 solution (Tab. S 4). After measuring the initial baseline, biotinylated liposomes were allowed
740 to bind the biosensor. Another baseline was measured in the same tube as before. For

741 association, 200 µl solutions of His-MinD and variants in different concentrations,
742 respectively, were exposed to the sensor, first without and later with addition of 2 mM Mg-
743 $^{2+}$ATP (final concentration) just before use. Furthermore, unspecific binding to liposome-
744 saturated sensors was tested using bovine serum albumin (BSA, 16 µM). For dissociation, the
745 sensor was exposed to buffer again. Each measurement was performed with a fresh
746 biosensor.

747 Kinetic analysis and fitting were performed by the BLItz Pro Software (version 1.3.1.3). Data
748 was exported and visualized using GraphPad Prism version 9.4.0 for Windows, (GraphPad
749 Software).

750 The BLItz Pro Software analysis follows a 1:1 binding model, where:

751 $$A + B \underset{k_{\mathrm{off}}}{\overset{k_{\mathrm{on}}}{\longleftrightarrow}} AB$$

752 with k_{on} = rate of association or "on-rate" and k_{off} = rate of dissociation or "off-rate".

753 Formula for fitting the association (a = slope):

754 $$Y = Y_0 + a\,(1 - e^{-k_{\mathrm{obs}} \times t})$$

755 $$k_{\mathrm{obs}} = k_{\mathrm{on}} \times [A(M)] + k_{\mathrm{off}}$$

756 Formula for fitting the dissociation:

757 $$Y = Y_0 + a \times e^{-k_{\mathrm{off}} \times t}$$

758 Resulting in the equilibrium dissociation constant K_D:

759 $$K_{\mathrm{D}} = \frac{k_{\mathrm{off}}}{k_{\mathrm{on}}}$$

760

761 **Fluorescence microscopy**

762 **Microscopy slide preparation**

763 For epifluorescence imaging, *B. subtilis* cells were mounted on 1.5% MD agarose pads using
764 1.5 x 1.6 cm "Gene Frames" (Thermo Scientific), and incubated 10 min at 37°C before
765 microscopic analysis.

766 For SMLM, slides and coverslips were first cleaned by overnight storage in 1 M KOH, carefully
767 rinsed with ddH2O, and subsequently dried with pressurized air. Next, 1.5% (w/v) low melting
768 agarose (Sigma-Aldrich) was dissolved in MD medium. Medium was sterile filtered (0.2 µm
769 pore size) shortly before being used to remove particles. To produce flat, uniform, and
770 reproducible agarose pads, 1.5 x 1.6 cm "Gene Frames" (Thermo Fisher) were utilized, and
771 pads were allowed to solidify for 1 h at room temperature to be used within the next 3 h.

772 **Staining of HaloTag**

773 For staining, 1 mL of bacterial culture was moved to a 2 mL microcentrifuge tube and
774 incubated with 5 nM (SMLM) or 50 nM (epifluorescence) HaloTag TMR ligand at 37 ◦C for 10
775 min. Cells were harvested (4000 g, 3 min, 37 °C) and washed four times in pre-warmed MD
776 medium, before being mounted on the previously described microscopy slides.

777 **Epifluorescence imaging**

778 For strain characterization (Fig. 2 B), microscopy images were taken on a Axio Observer 7
779 microscope (Zeiss) equipped with a Colibri 7 LED light source (Zeiss) and an OrcaR^2 camera
780 (Hamamatsu) using a Plan-Apochromat 100×/1.4 oil Ph3 objective (Zeiss). TMR fluorescence
781 was visualized with a 90 HE LED filter set (QBP 425/30 + 514/30 + 592/30 + 709/100)(Zeiss)
782 and excited at 555 nm (100% intensity of Colibri 7 LED) for 400 ms. The microscope was

783 equipped with an environmental chamber set to 37 °C. Digital images were acquired with Zen
784 Blue (Zeiss) and analyzed and edited with Fiji (104) ImageJ2 (105).

785 **SMLM imaging**

786 SMLM imaging was performed with an Elyra 7 (Zeiss) inverted microscope equipped with two
787 pco.edge sCMOS 4.2 CL HS cameras (PCO AG), connected through a DuoLink (Zeiss), only one
788 of which was used in this study. Cells were observed through an alpha Plan-Apochromat
789 63x/1.46 Oil Korr M27 Var2 objective, yielding a final pixel size of 97 nm. During image
790 acquisition, the focus was maintained with the help of a Definite Focus.2 system (Zeiss).
791 Fluorescence was excited with a 561 nm (100 mW) laser, and signals were observed through
792 a multiple beam splitter (405/488/561/641 nm) and laser block filters (405/488/561/641 nm)
793 followed by a Duolink SR QUAD (Zeiss) filter module (secondary beam splitter: LP 560,
794 emission filters: EF BP420-480 + BP495-550).

795 Cells were illuminated with the 561 nm laser (50% intensity) in TIRF mode (62° angle). For each
796 time lapse series 10000 frames were taken with 20 ms exposure time (~24 ms with transfer
797 time included) and 50% 561 nm intensity laser.

798 **SMLM analysis**

799 For average localization analysis (Fig. 4 A), a single-molecule localization table was constructed
800 from a 2D Gaussian fitting in the ZEN 3.0 SR (black) software (Zeiss) with a peak mask size of
801 9 and a peak intensity-to-noise ratio of 6, and further allowing molecules to overlap. Filtering
802 was used to minimize noise, background, and out-of-focus emitters, discarding events that did
803 not emit within a Point spread function size (PSF) of 100-200 nm and did not display a photon
804 count of 50-600. Further analysis was performed using individual Fiji (104) scripts for the cell
805 outlines and R (4.2.2) scripts in R Studio (2023.12.1+402) for the corresponding localization

806 events (75, 76). Here, the remaining events were transformed to align the orientation of all
807 cells in which the signals were detected, to be able to summarize all recorded localizations in
808 one normalized cell per strain. The localization frequency is displayed as a heatmap using the
809 gradual viridis scaling from the ggplot2 R package (106), where the highest frequency
810 (normalized frequency 1) is displayed in yellow and the lowest frequency (normalized
811 frequency 0) in blue (Fig. 4 A).

812 For single-molecule tracking, spots were identified with the LoG Detector of TrackMate v6.0.1
813 (107) implemented in Fiji 1.53 g (104), an estimated diameter of 0.5 µm, and median filter and
814 sub-pixel localization activated. The signal-to-noise threshold for the identification of the
815 spots was set at 7. To limit the detection of particles to single-molecules, frames belonging to
816 the bleaching phase of TMR were removed individually from the time lapses prior to the
817 identification of spots. Spots were merged into tracks via the "Simple LAP Tracker" of
818 TrackMate, with a maximum linking distance of 500 nm and no frame gaps allowed. Only
819 tracks with a minimum length of 5 frames were used for further analysis, yielding a minimum
820 number of total tracks per sample of 2596.

821 To identify differences in protein mobility and/or behavior, the resulting tracks were subjected
822 to stationary localization analysis (SLA), mean-squared-displacement (MSD) and square
823 displacement (SQD) analysis in SMTracker 2.0 (73). SLA analysis was performed with a
824 confinement circle radius of 97 nm and a minimum number of 5 steps to be considered static.
825 The average MSD was calculated for four separate time points per strain (exposure of 20 ms -
826 τ = 24, 48, 72 and 96 ms), followed by fitting of the data to a linear equation. The last time
827 point of each track was excluded to avoid track-ending-related artifacts. The cumulative
828 probability distribution of the square displacements (SQD) was used to estimate the diffusion
829 constants and relative fractions of up to three diffusive states. Diffusion constants were

830 determined simultaneously for the compared conditions, therefore allowing for a more direct
831 population fractions comparison. Additionally, the analysis was performed for each strain non-
832 comparatively, yielding individual diffusion coefficients, displayed in Tab. 2.

Acknowledgments

This research was supported by the Deutsche Forschungsgemeinschaft (DFG) within the Transregio Collaborative Research Center (TRR 174) “Spatiotemporal Dynamics of Bacterial Cells”. We thank Leendert Hamoen (Amsterdam) and Henrik Strahl (Newcastle) for communicating unpublished results prior to publication. We are also grateful to Anna Becker and Vivian Hennig (Kiel) for help in the initial stages of this project as part of their BSc theses.

Author Contributions

M.B. and H.F. conceived the study, H.F. constructed the strains, performed the in vivo and in vitro experiments incl. microscopy. H.F. and M.B. analyzed the data and wrote the manuscript.

Declaration of Interests

The authors declare no competing interests.

850 # References
851

852 1. Kotak S, Gonczy P. 2013. Mechanisms of spindle positioning: cortical force generators in the
853 limelight. Curr Opin Cell Biol 25:741-8.
854 2. Pollard TD, O'Shaughnessy B. 2019. Molecular Mechanism of Cytokinesis. Annu Rev Biochem
855 88:661-689.
856 3. Cameron TA, Margolin W. 2024. Insights into the assembly and regulation of the bacterial
857 divisome. Nat Rev Microbiol 22:33-45.
858 4. Mahone CR, Goley ED. 2020. Bacterial cell division at a glance. J Cell Sci 133.
859 5. den Blaauwen T, Hamoen LW, Levin PA. 2017. The divisome at 25: the road ahead. Curr Opin
860 Microbiol 36:85-94.
861 6. Bi EF, Lutkenhaus J. 1991. FtsZ ring structure associated with division in Escherichia coli.
862 Nature 354:161-4.
863 7. Lowe J, Amos LA. 1998. Crystal structure of the bacterial cell-division protein FtsZ. Nature
864 391:203-6.
865 8. Schaper S, Brito AD, Saraiva BM, Squyres GR, Holmes MJ, Garner EC, Hensel Z, Henriques R,
866 Pinho MG. 2024. Cell constriction requires processive septal peptidoglycan synthase
867 movement independent of FtsZ treadmilling in Staphylococcus aureus. Nat Microbiol 9:1049-
868 1063.
869 9. Whitley KD, Jukes C, Tregidgo N, Karinou E, Almada P, Cesbron Y, Henriques R, Dekker C,
870 Holden S. 2021. FtsZ treadmilling is essential for Z-ring condensation and septal constriction
871 initiation in Bacillus subtilis cell division. Nat Commun 12:2448.
872 10. Squyres GR, Holmes MJ, Barger SR, Pennycook BR, Ryan J, Yan VT, Garner EC. 2021. Single-
873 molecule imaging reveals that Z-ring condensation is essential for cell division in Bacillus
874 subtilis. Nat Microbiol 6:553-562.
875 11. Egan AJF, Errington J, Vollmer W. 2020. Regulation of peptidoglycan synthesis and
876 remodelling. Nat Rev Microbiol 18:446-460.
877 12. Adams DW, Errington J. 2009. Bacterial cell division: assembly, maintenance and disassembly
878 of the Z ring. Nat Rev Microbiol 7:642-53.
879 13. Chan H, Mohamed AMT, Grainge I, Rodrigues CDA. 2022. FtsK and SpoIIIE, coordinators of
880 chromosome segregation and envelope remodeling in bacteria. Trends Microbiol 30:480-
881 494.
882 14. Reyes-Lamothe R, Sherratt DJ. 2019. The bacterial cell cycle, chromosome inheritance and
883 cell growth. Nat Rev Microbiol 17:467-478.
884 15. Bramkamp M, van Baarle S. 2009. Division site selection in rod-shaped bacteria. Curr Opin
885 Microbiol 12:683-8.
886 16. Szwedziak P, Ghosal D. 2017. FtsZ-ring Architecture and Its Control by MinCD. Subcell
887 Biochem 84:213-244.
888 17. Ortiz C, Natale P, Cueto L, Vicente M. 2016. The keepers of the ring: regulators of FtsZ
889 assembly. FEMS Microbiol Rev 40:57-67.
890 18. Wu LJ, Errington J. 2011. Nucleoid occlusion and bacterial cell division. Nat Rev Microbiol
891 10:8-12.
892 19. Bernhardt TG, de Boer PA. 2005. SlmA, a nucleoid-associated, FtsZ binding protein required
893 for blocking septal ring assembly over Chromosomes in E. coli. Mol Cell 18:555-64.
894 20. Cho H, McManus HR, Dove SL, Bernhardt TG. 2011. Nucleoid occlusion factor SlmA is a DNA-
895 activated FtsZ polymerization antagonist. Proc Natl Acad Sci U S A 108:3773-8.
896 21. Tonthat NK, Arold ST, Pickering BF, Van Dyke MW, Liang S, Lu Y, Beuria TK, Margolin W,
897 Schumacher MA. 2011. Molecular mechanism by which the nucleoid occlusion factor, SlmA,
898 keeps cytokinesis in check. EMBO J 30:154-64.
899 22. Wu LJ, Errington J. 2004. Coordination of cell division and chromosome segregation by a
900 nucleoid occlusion protein in Bacillus subtilis. Cell 117:915-25.

901 23. Wu LJ, Ishikawa S, Kawai Y, Oshima T, Ogasawara N, Errington J. 2009. Noc protein binds to
902 specific DNA sequences to coordinate cell division with chromosome segregation. EMBO J
903 28:1940-52.
904 24. Jalal ASB, Tran NT, Wu LJ, Ramakrishnan K, Rejzek M, Gobbato G, Stevenson CEM, Lawson
905 DM, Errington J, Le TBK. 2021. CTP regulates membrane-binding activity of the nucleoid
906 occlusion protein Noc. Mol Cell 81:3623-3636 e6.
907 25. Adams DW, Wu LJ, Errington J. 2015. Nucleoid occlusion protein Noc recruits DNA to the
908 bacterial cell membrane. EMBO J 34:491-501.
909 26. Adler HI, Fisher WD, Cohen A, Hardigree AA. 1967. MINIATURE escherichia coli CELLS
910 DEFICIENT IN DNA. Proc Natl Acad Sci U S A 57:321-6.
911 27. Schaumberg TH, Kuempel PL. 1983. Genetic mapping of the minB locus in Escherichia coli K-
912 12. J Bacteriol 153:1063-5.
913 28. Davie E, Sydnor K, Rothfield LI. 1984. Genetic basis of minicell formation in Escherichia coli K-
914 12. J Bacteriol 158:1202-3.
915 29. de Boer PA, Crossley RE, Rothfield LI. 1989. A division inhibitor and a topological specificity
916 factor coded for by the minicell locus determine proper placement of the division septum in
917 E. coli. Cell 56:641-9.
918 30. de Boer PA, Crossley RE, Rothfield LI. 1992. Roles of MinC and MinD in the site-specific
919 septation block mediated by the MinCDE system of Escherichia coli. J Bacteriol 174:63-70.
920 31. Hu Z, Mukherjee A, Pichoff S, Lutkenhaus J. 1999. The MinC component of the division site
921 selection system in Escherichia coli interacts with FtsZ to prevent polymerization. Proc Natl
922 Acad Sci U S A 96:14819-24.
923 32. Cordell SC, Anderson RE, Lowe J. 2001. Crystal structure of the bacterial cell division inhibitor
924 MinC. EMBO J 20:2454-61.
925 33. Hu Z, Lutkenhaus J. 2000. Analysis of MinC reveals two independent domains involved in
926 interaction with MinD and FtsZ. J Bacteriol 182:3965-71.
927 34. Shen B, Lutkenhaus J. 2009. The conserved C-terminal tail of FtsZ is required for the septal
928 localization and division inhibitory activity of MinC(C)/MinD. Mol Microbiol 72:410-24.
929 35. Shen B, Lutkenhaus J. 2010. Examination of the interaction between FtsZ and MinCN in E. coli
930 suggests how MinC disrupts Z rings. Mol Microbiol 75:1285-98.
931 36. Marston AL, Errington J. 1999. Selection of the midcell division site in Bacillus subtilis through
932 MinD-dependent polar localization and activation of MinC. Mol Microbiol 33:84-96.
933 37. Gregory JA, Becker EC, Pogliano K. 2008. Bacillus subtilis MinC destabilizes FtsZ-rings at new
934 cell poles and contributes to the timing of cell division. Genes Dev 22:3475-88.
935 38. Scheffers DJ. 2008. The effect of MinC on FtsZ polymerization is pH dependent and can be
936 counteracted by ZapA. FEBS Lett 582:2601-8.
937 39. de Boer PA, Crossley RE, Hand AR, Rothfield LI. 1991. The MinD protein is a membrane
938 ATPase required for the correct placement of the Escherichia coli division site. EMBO J
939 10:4371-80.
940 40. Marston AL, Thomaides HB, Edwards DH, Sharpe ME, Errington J. 1998. Polar localization of
941 the MinD protein of Bacillus subtilis and its role in selection of the mid-cell division site.
942 Genes Dev 12:3419-30.
943 41. Pulianmackal LT, Vecchiarelli AG. 2024. Positioning of cellular components by the ParA/MinD
944 family of ATPases. Curr Opin Microbiol 79:102485.
945 42. Lutkenhaus J. 2012. The ParA/MinD family puts things in their place. Trends Microbiol
946 20:411-8.
947 43. Szardenings F, Guymer D, Gerdes K. 2011. ParA ATPases can move and position DNA and
948 subcellular structures. Curr Opin Microbiol 14:712-8.
949 44. Szeto TH, Rowland SL, Habrukowich CL, King GF. 2003. The MinD membrane targeting
950 sequence is a transplantable lipid-binding helix. J Biol Chem 278:40050-6.

951 45. Szeto TH, Rowland SL, Rothfield LI, King GF. 2002. Membrane localization of MinD is
952 mediated by a C-terminal motif that is conserved across eubacteria, archaea, and
953 chloroplasts. Proc Natl Acad Sci U S A 99:15693-8.
954 46. Zhou H, Lutkenhaus J. 2004. The switch I and II regions of MinD are required for binding and
955 activating MinC. J Bacteriol 186:1546-55.
956 47. Raskin DM, de Boer PA. 1999. Rapid pole-to-pole oscillation of a protein required for
957 directing division to the middle of Escherichia coli. Proc Natl Acad Sci U S A 96:4971-6.
958 48. Hale CA, Meinhardt H, de Boer PA. 2001. Dynamic localization cycle of the cell division
959 regulator MinE in Escherichia coli. EMBO J 20:1563-72.
960 49. Hu Z, Lutkenhaus J. 1999. Topological regulation of cell division in Escherichia coli involves
961 rapid pole to pole oscillation of the division inhibitor MinC under the control of MinD and
962 MinE. Mol Microbiol 34:82-90.
963 50. Loose M, Fischer-Friedrich E, Ries J, Kruse K, Schwille P. 2008. Spatial regulators for bacterial
964 cell division self-organize into surface waves in vitro. Science 320:789-92.
965 51. Varley AW, Stewart GC. 1992. The divIVB region of the Bacillus subtilis chromosome encodes
966 homologs of Escherichia coli septum placement (minCD) and cell shape (mreBCD)
967 determinants. J Bacteriol 174:6729-42.
968 52. Levin PA, Margolis PS, Setlow P, Losick R, Sun D. 1992. Identification of Bacillus subtilis genes
969 for septum placement and shape determination. J Bacteriol 174:6717-28.
970 53. Lee S, Price CW. 1993. The minCD locus of Bacillus subtilis lacks the minE determinant that
971 provides topological specificity to cell division. Mol Microbiol 7:601-10.
972 54. Patrick JE, Kearns DB. 2008. MinJ (YvjD) is a topological determinant of cell division in Bacillus
973 subtilis. Mol Microbiol 70:1166-79.
974 55. Bramkamp M, Emmins R, Weston L, Donovan C, Daniel RA, Errington J. 2008. A novel
975 component of the division-site selection system of Bacillus subtilis and a new mode of action
976 for the division inhibitor MinCD. Mol Microbiol 70:1556-69.
977 56. van Baarle S, Bramkamp M. 2010. The MinCDJ system in Bacillus subtilis prevents minicell
978 formation by promoting divisome disassembly. PLoS One 5:e9850.
979 57. Yu Y, Zhou J, Dempwolff F, Baker JD, Kearns DB, Jacobson SC. 2020. The Min System
980 Disassembles FtsZ Foci and Inhibits Polar Peptidoglycan Remodeling in Bacillus subtilis. mBio
981 11.
982 58. Bach JN, Albrecht N, Bramkamp M. 2014. Imaging DivIVA dynamics using photo-convertible
983 and activatable fluorophores in Bacillus subtilis. Front Microbiol 5:59.
984 59. Giacomelli G, Feddersen H, Peng F, Martins GB, Grafemeyer M, Meyer F, Mayer B, Graumann
985 PL, Bramkamp M. 2022. Subcellular Dynamics of a Conserved Bacterial Polar Scaffold Protein.
986 Genes (Basel) 13.
987 60. Feddersen H, Wurthner L, Frey E, Bramkamp M. 2021. Dynamics of the Bacillus subtilis Min
988 System. mBio 12.
989 61. Ishikawa K, Matsuoka S, Hara H, Matsumoto K. 2017. Septal membrane localization by C-
990 terminal amphipathic alpha-helices of MinD in Bacillus subtilis mutant cells lacking MinJ or
991 DivIVA. Genes Genet Syst 92:81-98.
992 62. Ramm B, Glock P, Schwille P. 2018. In Vitro Reconstitution of Self-Organizing Protein Patterns
993 on Supported Lipid Bilayers. J Vis Exp doi:10.3791/58139.
994 63. Hu Z, Lutkenhaus J. 2001. Topological regulation of cell division in *E. coli*: Spatiotemporal
995 oscillation of MinD requires stimulation of its ATPase by MinE and phospholipid. Mol Cell
996 7:1337-43.
997 64. Hu Z, Lutkenhaus J. 2003. A conserved sequence at the C-terminus of MinD is required for
998 binding to the membrane and targeting MinC to the septum. Mol Microbiol 47:345-55.
999 65. Heermann T, Ramm B, Glaser S, Schwille P. 2020. Local Self-Enhancement of MinD
1000 Membrane Binding in Min Protein Pattern Formation. J Mol Biol 432:3191-3204.
1001 66. Strahl H, Hamoen LW. 2010. Membrane potential is important for bacterial cell division. Proc
1002 Natl Acad Sci U S A 107:12281-6.

1003 67. Karoui ME, Errington J. 2001. Isolation and characterization of topological specificity mutants
1004 of minD in Bacillus subtilis. Mol Microbiol 42:1211-21.
1005 68. Leonard TA, Butler PJ, Lowe J. 2005. Bacterial chromosome segregation: structure and DNA
1006 binding of the Soj dimer--a conserved biological switch. EMBO J 24:270-82.
1007 69. Wu W, Park KT, Holyoak T, Lutkenhaus J. 2011. Determination of the structure of the MinD-
1008 ATP complex reveals the orientation of MinD on the membrane and the relative location of
1009 the binding sites for MinE and MinC. Mol Microbiol 79:1515-28.
1010 70. Maximova K, Reuter N, Trylska J. 2019. Peptidomimetic inhibitors targeting the membrane-
1011 binding site of the neutrophil proteinase 3. Biochim Biophys Acta Biomembr 1861:1502-
1012 1509.
1013 71. Wallner J, Lhota G, Schosserer M, Vorauer-Uhl K. 2017. An approach for liposome
1014 immobilization using sterically stabilized micelles (SSMs) as a precursor for bio-layer
1015 interferometry-based interaction studies. Colloids Surf B Biointerfaces 154:186-194.
1016 72. Lackner LL, Raskin DM, de Boer PA. 2003. ATP-dependent interactions between Escherichia
1017 coli Min proteins and the phospholipid membrane in vitro. J Bacteriol 185:735-49.
1018 73. Oviedo-Bocanegra LM, Hinrichs R, Rotter DAO, Dersch S, Graumann PL. 2021. Single
1019 molecule/particle tracking analysis program SMTracker 2.0 reveals different dynamics of
1020 proteins within the RNA degradosome complex in Bacillus subtilis. Nucleic Acids Res 49:e112.
1021 74. Ershov D, Phan MS, Pylvanainen JW, Rigaud SU, Le Blanc L, Charles-Orszag A, Conway JRW,
1022 Laine RF, Roy NH, Bonazzi D, Dumenil G, Jacquemet G, Tinevez JY. 2022. TrackMate 7:
1023 integrating state-of-the-art segmentation algorithms into tracking pipelines. Nat Methods
1024 19:829-832.
1025 75. R Core Team. 2022. R: A Language and Environment for Statistical Computing. R Foundation
1026 for Statistical Computing:Vienna, Austria. https://www.R-project.org/.
1027 76. Posit team. 2024. RStudio: Integrated Development Environment for R. Posit Software, PBC;
1028 Boston, MA; http://wwwpositco/.
1029 77. Heermann T, Steiert F, Ramm B, Hundt N, Schwille P. 2021. Mass-sensitive particle tracking
1030 to elucidate the membrane-associated MinDE reaction cycle. Nat Methods 18:1239-1246.
1031 78. Barak LS, Webb WW. 1982. Diffusion of low density lipoprotein-receptor complex on human
1032 fibroblasts. J Cell Biol 95:846-52.
1033 79. Goulian M, Simon SM. 2000. Tracking single proteins within cells. Biophys J 79:2188-98.
1034 80. Weimann L, Ganzinger KA, McColl J, Irvine KL, Davis SJ, Gay NJ, Bryant CE, Klenerman D.
1035 2013. A quantitative comparison of single-dye tracking analysis tools using Monte Carlo
1036 simulations. PLoS One 8:e64287.
1037 81. Landge AN, Jordan BM, Diego X, Muller P. 2020. Pattern formation mechanisms of self-
1038 organizing reaction-diffusion systems. Dev Biol 460:2-11.
1039 82. St Johnston D, Nusslein-Volhard C. 1992. The origin of pattern and polarity in the Drosophila
1040 embryo. Cell 68:201-19.
1041 83. Negrete J, Jr., Oates AC. 2021. Towards a physical understanding of developmental
1042 patterning. Nat Rev Genet 22:518-531.
1043 84. Turing AM. 1990. The chemical basis of morphogenesis. 1953. Bull Math Biol 52:153-97;
1044 discussion 119-52.
1045 85. Meinhardt H, Gierer A. 2000. Pattern formation by local self-activation and lateral inhibition.
1046 Bioessays 22:753-60.
1047 86. Rowlett VW, Margolin W. 2013. The bacterial Min system. Curr Biol 23:R553-6.
1048 87. Ramm B, Heermann T, Schwille P. 2019. The E. coli MinCDE system in the regulation of
1049 protein patterns and gradients. Cell Mol Life Sci 76:4245-4273.
1050 88. Kretschmer S, Schwille P. 2016. Pattern formation on membranes and its role in bacterial cell
1051 division. Curr Opin Cell Biol 38:52-9.
1052 89. Halatek J, Brauns F, Frey E. 2018. Self-organization principles of intracellular pattern
1053 formation. Philos Trans R Soc Lond B Biol Sci 373.

1054 90. Scholefield G, Whiting R, Errington J, Murray H. 2011. Spo0J regulates the oligomeric state of
1055 Soj to trigger its switch from an activator to an inhibitor of DNA replication initiation. Mol
1056 Microbiol 79:1089-100.
1057 91. Easter J, Jr., Gober JW. 2002. ParB-stimulated nucleotide exchange regulates a switch in
1058 functionally distinct ParA activities. Mol Cell 10:427-34.
1059 92. Lim HC, Surovtsev IV, Beltran BG, Huang F, Bewersdorf J, Jacobs-Wagner C. 2014. Evidence
1060 for a DNA-relay mechanism in ParABS-mediated chromosome segregation. Elife 3:e02758.
1061 93. Loose M, Fischer-Friedrich E, Herold C, Kruse K, Schwille P. 2011. Min protein patterns
1062 emerge from rapid rebinding and membrane interaction of MinE. Nat Struct Mol Biol 18:577-
1063 83.
1064 94. Vecchiarelli AG, Li M, Mizuuchi M, Hwang LC, Seol Y, Neuman KC, Mizuuchi K. 2016.
1065 Membrane-bound MinDE complex acts as a toggle switch that drives Min oscillation coupled
1066 to cytoplasmic depletion of MinD. Proc Natl Acad Sci U S A 113:E1479-88.
1067 95. Turkowyd B, Virant D, Endesfelder U. 2016. From single molecules to life: microscopy at the
1068 nanoscale. Anal Bioanal Chem 408:6885-911.
1069 96. Yao Z, Carballido-Lopez R. 2014. Fluorescence imaging for bacterial cell biology: from
1070 localization to dynamics, from ensembles to single molecules. Annu Rev Microbiol 68:459-76.
1071 97. Miyagi A, Ramm B, Schwille P, Scheuring S. 2018. High-Speed Atomic Force Microscopy
1072 Reveals the Inner Workings of the MinDE Protein Oscillator. Nano Lett 18:288-296.
1073 98. Halatek J, Frey E. 2012. Highly canalized MinD transfer and MinE sequestration explain the
1074 origin of robust MinCDE-protein dynamics. Cell Rep 1:741-52.
1075 99. Bohorquez L, Strahl H, Marenduzzo D, Thiele M, Bürmann F, Hamoen L. 2024. Cyclical MinD
1076 membrane affinity differences are not necessary for MinD gradient formation in *Bacillus*
1077 *subtilis*. doi:10.1101/2024.06.11.598461. bioRxiv.
1078 100. Ghosal D, Trambaiolo D, Amos LA, Lowe J. 2014. MinCD cell division proteins form alternating
1079 copolymeric cytomotive filaments. Nat Commun 5:5341.
1080 101. Anagnostopoulos C, Spizizen J. 1961. Requirements for Transformation in *Bacillus subtilis*. J
1081 Bacteriol 81:741-6.
1082 102. Jumper J, Evans R, Pritzel A, Green T, Figurnov M, Ronneberger O, Tunyasuvunakool K, Bates
1083 R, Zidek A, Potapenko A, Bridgland A, Meyer C, Kohl SAA, Ballard AJ, Cowie A, Romera-
1084 Paredes B, Nikolov S, Jain R, Adler J, Back T, Petersen S, Reiman D, Clancy E, Zielinski M,
1085 Steinegger M, Pacholska M, Berghammer T, Bodenstein S, Silver D, Vinyals O, Senior AW,
1086 Kavukcuoglu K, Kohli P, Hassabis D. 2021. Highly accurate protein structure prediction with
1087 AlphaFold. Nature 596:583-589.
1088 103. Weiss M, Giacomelli G, Assaya MB, Grundt F, Haouz A, Peng F, Petrella S, Wehenkel AM,
1089 Bramkamp M. 2023. The MksG nuclease is the executing part of the bacterial plasmid
1090 defense system MksBEFG. Nucleic Acids Res 51:3288-3306.
1091 104. Schindelin J, Arganda-Carreras I, Frise E, Kaynig V, Longair M, Pietzsch T, Preibisch S, Rueden
1092 C, Saalfeld S, Schmid B, Tinevez J-Y, White DJ, Hartenstein V, Eliceiri K, Tomancak P, Cardona
1093 A. 2012. Fiji: an open-source platform for biological-image analysis. Nature Methods 9:676-
1094 682.
1095 105. Rueden CT, Schindelin J, Hiner MC, DeZonia BE, Walter AE, Arena ET, Eliceiri KW. 2017.
1096 ImageJ2: ImageJ for the next generation of scientific image data. BMC Bioinformatics 18:529.
1097 106. Wickham H. 2016. ggplot2: Elegant Graphics for Data Analysis. Springer-Verlag New
1098 York:ISBN 978-3-319-24277-4, https://ggplot2.tidyverse.org.
1099 107. Tinevez JY, Perry N, Schindelin J, Hoopes GM, Reynolds GD, Laplantine E, Bednarek SY, Shorte
1100 SL, Eliceiri KW. 2017. TrackMate: An open and extensible platform for single-particle tracking.
1101 Methods 115:80-90.